

Measurement of the Full Shape of the Thermal Sunyaev-Zel'dovich Power Spectrum from South Pole Telescope and *Herschel*-SPIRE Observations

S. RAGHUNATHAN,^{1, 2} P. A. R. ADE,³ D. ANBAJAGANE,^{4, 5} A. J. ANDERSON,^{6, 5, 4} B. ANSARINEJAD,⁷ M. ARCHIPLEY,^{4, 5} J. E. AUSTERMANN,^{8, 9} L. BALKENHOL,¹⁰ D. R. BARRON,¹¹ P. S. BARRY,¹² J. A. BEALL,⁸ K. BENABED,¹⁰ A. N. BENDER,^{13, 5, 4} B. A. BENSON,^{6, 5, 4} F. BIANCHINI,⁷ L. E. BLEEM,^{13, 5, 4} J. BOCK,^{14, 15} S. BOCQUET,¹⁶ F. R. BOUCHET,¹⁰ L. BRYANT,¹⁷ E. CAMPHUIS,¹⁰ M. G. CAMPITIELLO,¹³ J. E. CARLSTROM,^{5, 18, 13, 4, 17} J. CARRON,^{19, 20} C. L. CHANG,^{5, 13, 4} P. CHAUBAL,⁷ H. C. CHIANG,^{21, 22} P. M. CHICHURA,^{18, 5} A. CHOKSHI,⁴ T.-L. CHOU,^{4, 5, 23} R. CITRON,²⁴ A. COERVER,²⁵ C. CORBETT MORAN,²⁶ T. M. CRAWFORD,^{4, 5} A. T. CRITES,^{5, 4, 27, 28} C. DALEY,^{29, 30} T. DE HAAN,^{25, 31} K. R. DIBERT,^{4, 5} M. A. DOBBS,^{21, 32} M. DOOHAN,⁷ A. DOUSSOT,¹⁰ D. DUTCHER,³³ W. EVERETT,³⁴ C. FENG,^{35, 36, 37} K. R. FERGUSON,^{38, 39} N. C. FERREE,^{40, 41, 42} K. FICHMAN,^{18, 5} A. FOSTER,³³ S. GALLI,¹⁰ J. GALLICCHIO,^{5, 43} A. E. GAMBREL,⁵ A. K. GAO,³⁷ R. W. GARDNER,¹⁷ F. GE,^{40, 41, 42, 1} E. M. GEORGE,^{44, 25} N. GOECKNER-WALD,^{42, 41} R. GUALTIERI,^{13, 45} F. GUIDI,^{1, 10} S. GUNS,²⁵ N. GUPTA,⁷ N. W. HALVERSON,^{34, 9} E. HIVON,¹⁰ A. Y. Q. HO,⁴⁶ G. P. HOLDER,^{30, 37, 32} W. L. HOLZAPFEL,²⁵ J. C. HOOD,⁵ J. D. HRUBES,²⁴ A. HRYCIUK,^{18, 5} N. HUANG,²⁵ J. HUBMAYR,⁸ K. D. IRWIN,^{47, 42} T. JHAVERI,^{4, 5} F. KERUZOZÉ,¹³ A. R. KHALIFE,¹⁰ L. KNOX,⁴⁸ M. KORMAN,⁴⁹ K. KORNOELJE,^{4, 5, 13} C.-L. KUO,^{41, 42, 47} A. T. LEE,^{25, 31} K. LEVY,⁷ Y. LI,⁵ D. LI,^{8, 47} A. E. LOWITZ,⁵ A. LOWITZ,⁴ C. LU,³⁷ G. P. LYNCH,¹ T. J. MACCARONE,⁵⁰ A. S. MANIYAR,^{41, 42, 47} E. S. MARTSEN,^{4, 5} J. J. McMAHON,^{5, 18, 4} F. MENANTEAU,^{30, 2} M. MILLEA,²⁵ J. MONTGOMERY,²¹ Y. NAKATO,⁴² T. NATOLI,^{4, 5, 27} J. P. NIBARGER,⁸ G. I. NOBLE,^{27, 28} V. NOVOSAD,⁵¹ Y. OMORI,^{4, 5} A. OUELLETTE,³⁷ S. PADIN,^{5, 4, 40} Z. PAN,^{13, 5, 18} P. PASCHOS,¹⁷ S. PATIL,⁷ K. A. PHADKE,^{30, 2, 52} A. W. POLLAK,⁴ K. PRABHU,¹ C. PRYKE,⁵³ W. QUAN,^{13, 18, 5} M. RAHIMI,⁷ A. RAHLIN,^{4, 5} C. L. REICHARDT,⁷ M. ROUBLE,²¹ J. E. RUHL,⁴⁹ B. R. SALIWANCHIK,^{49, 54} K. K. SCHAFER,^{5, 17, 55} E. SCHIAPPUCCI,⁷ C. SIEVERS,²⁴ A. C. SILVA OLIVEIRA,^{40, 41, 42} A. SIMPSON,^{4, 5} G. SMECHER,^{21, 56} J. A. SOBRIN,^{6, 5} A. A. STARK,⁵⁷ J. STEPHEN,¹⁷ C. TANDOI,³⁰ B. THORNE,¹ C. TRENDAFILOVA,² C. TUCKER,³ C. UMILTA,³⁷ T. VEECH,⁵⁸ J. D. VIEIRA,^{30, 37} A. G. VIEREGG,^{5, 4, 17, 18} M. P. VIERO,¹⁴ A. VITRIER,¹⁰ Y. WAN,^{30, 2} G. WANG,¹³ N. WHITEHORN,³⁹ W. L. K. WU,^{40, 47, 5} V. YEFREMENKO,¹³ M. R. YOUNG,^{6, 5} J. A. ZEBROWSKI²⁵ AND M. ZEMCOV^{59, 15}

(SPTpol AND SPT-3G COLLABORATION)

¹Department of Physics & Astronomy, University of California, One Shields Avenue, Davis, CA 95616, USA

²Center for AstroPhysical Surveys, National Center for Supercomputing Applications, Urbana, IL, 61801, USA

³School of Physics and Astronomy, Cardiff University, Cardiff CF24 3YB, United Kingdom

⁴Department of Astronomy and Astrophysics, University of Chicago, 5640 South Ellis Avenue, Chicago, IL, 60637, USA

⁵Kavli Institute for Cosmological Physics, University of Chicago, 5640 South Ellis Avenue, Chicago, IL, 60637, USA

⁶Fermi National Accelerator Laboratory, MS209, P.O. Box 500, Batavia, IL, 60510, USA

⁷School of Physics, University of Melbourne, Parkville, VIC 3010, Australia

⁸NIST Quantum Devices Group, 325 Broadway Mailcode 817.03, Boulder, CO, 80305, USA

⁹Department of Physics, University of Colorado, Boulder, CO, 80309, USA

¹⁰Sorbonne Université, CNRS, UMR 7095, Institut d'Astrophysique de Paris, 98 bis bd Arago, 75014 Paris, France

¹¹Department of Physics and Astronomy, University of New Mexico, Albuquerque, NM, 87131, USA

¹²School of Physics and Astronomy, Cardiff University, Cardiff, CF24 3AA, UK

¹³High-Energy Physics Division, Argonne National Laboratory, 9700 South Cass Avenue, Lemont, IL, 60439, USA

¹⁴California Institute of Technology, Pasadena, CA 91125, USA

¹⁵Jet Propulsion Laboratory, California Institute of Technology, Pasadena, CA 91109, USA

¹⁶University Observatory, Faculty of Physics, Ludwig-Maximilians-Universität, Scheinerstr. 1, 81679 Munich, Germany

¹⁷Enrico Fermi Institute, University of Chicago, 5640 South Ellis Avenue, Chicago, IL, 60637, USA

¹⁸Department of Physics, University of Chicago, 5640 South Ellis Avenue, Chicago, IL, 60637, USA

¹⁹Université de Genève, Département de Physique Théorique, 24 Quai Ansermet, CH-1211 Genève 4, Switzerland

²⁰Department of Physics & Astronomy, University of Sussex, Brighton BN1 9QH, UK

²¹Department of Physics and McGill Space Institute, McGill University, 3600 Rue University, Montreal, Quebec H3A 2T8, Canada

²²School of Mathematics, Statistics & Computer Science, University of KwaZulu-Natal, Durban, South Africa

²³National Taiwan University, No. 1, Sec. 4, Roosevelt Road, Taipei 106319, Taiwan

²⁴University of Chicago, 5640 South Ellis Avenue, Chicago, IL, 60637, USA

²⁵Department of Physics, University of California, Berkeley, CA, 94720, USA

²⁶Jet Propulsion Laboratory, Pasadena, CA 91109, USA

²⁷Dunlap Institute for Astronomy & Astrophysics, University of Toronto, 50 St. George Street, Toronto, ON, M5S 3H4, Canada

²⁸David A. Dunlap Department of Astronomy & Astrophysics, University of Toronto, 50 St. George Street, Toronto, ON, M5S 3H4, Canada

²⁹Université Paris-Saclay, Université Paris Cité, CEA, CNRS, AIM, 91191, Gif-sur-Yvette, France

³⁰Department of Astronomy, University of Illinois Urbana-Champaign, 1002 West Green Street, Urbana, IL, 61801, USA

³¹Physics Division, Lawrence Berkeley National Laboratory, Berkeley, CA, 94720, USA

³²Canadian Institute for Advanced Research, CIFAR Program in Gravity and the Extreme Universe, Toronto, ON, M5G 1Z8, Canada

³³Joseph Henry Laboratories of Physics, Jadwin Hall, Princeton University, Princeton, NJ 08544, USA

³⁴Department of Astrophysical and Planetary Sciences, University of Colorado, Boulder, CO, 80309, USA

³⁵Department of Astronomy, University of Science and Technology of China, Hefei 230026, China

³⁶School of Astronomy and Space Science, University of Science and Technology of China, Hefei 230026

³⁷Department of Physics, University of Illinois Urbana-Champaign, 1110 West Green Street, Urbana, IL, 61801, USA

³⁸Department of Physics and Astronomy, University of California, Los Angeles, CA, 90095, USA

³⁹Department of Physics and Astronomy, Michigan State University, East Lansing, MI 48824, USA

⁴⁰California Institute of Technology, 1200 East California Boulevard, Pasadena, CA, 91125, USA

⁴¹Kavli Institute for Particle Astrophysics and Cosmology, Stanford University, 452 Lomita Mall, Stanford, CA, 94305, USA

⁴²Department of Physics, Stanford University, 382 Via Pueblo Mall, Stanford, CA, 94305, USA

⁴³Harvey Mudd College, 301 Platt Boulevard, Claremont, CA, 91711, USA

⁴⁴European Southern Observatory, Karl-Schwarzschild-Str. 2, 85748 Garching bei München, Germany

⁴⁵Department of Physics and Astronomy, Northwestern University, 633 Clark St, Evanston, IL, 60208, USA

⁴⁶Department of Astronomy, Cornell University, Ithaca, NY 14853, USA

⁴⁷SLAC National Accelerator Laboratory, 2575 Sand Hill Road, Menlo Park, CA, 94025, USA

⁴⁸Department of Physics, University of California, One Shields Avenue, Davis, CA, 95616, USA

⁴⁹Department of Physics, Case Western Reserve University, Cleveland, OH, 44106, USA

⁵⁰Department of Physics & Astronomy, Box 41051, Texas Tech University, Lubbock TX 79409-1051, USA

⁵¹Materials Sciences Division, Argonne National Laboratory, 9700 South Cass Avenue, Lemont, IL, 60439, USA

⁵²NSF-Simons AI Institute for the Sky (SkAI), 172 E. Chestnut St., Chicago, IL 60611, USA

⁵³School of Physics and Astronomy, University of Minnesota, 116 Church Street SE Minneapolis, MN, 55455, USA

⁵⁴Department of Physics, Yale University, P.O. Box 208120, New Haven, CT 06520-8120

⁵⁵Liberal Arts Department, School of the Art Institute of Chicago, 112 South Michigan Avenue, Chicago, IL, 60603, USA

⁵⁶Three-Speed Logic, Inc., Victoria, B.C., V8S 3Z5, Canada

⁵⁷Center for Astrophysics / Harvard & Smithsonian, 60 Garden Street, Cambridge, MA, 02138, USA

⁵⁸Space Science and Engineering Division, Southwest Research Institute, San Antonio, TX 78238

⁵⁹School of Physics and Astronomy, Rochester Institute of Technology, Rochester, NY 14623, USA

ABSTRACT

We present a measurement of the full shape of the power spectrum of the thermal Sunyaev-Zel'dovich (tSZ) effect down to arcminute scales using cosmic microwave background (CMB) data from the South Pole Telescope (SPT) over roughly 100 deg² field. The analysis incorporates data from the 2019/20 seasons of the SPT-3G survey in bands centered at 95, 150, and 220 GHz; from the full SPTpol dataset at 150 GHz; and from *Herschel*-SPIRE survey in bands centered at 600 and 857 GHz. We combine data from all the above bands using linear combination (LC) techniques to produce a tSZ or Compton- y map. We modify the LC weights to produce multiple versions of the Compton- y map, including minimum-variance (MV) and foreground-minimized (-min) maps. We measure the auto- and cross-spectra of a subset of these maps in the range $\ell \in [500, 5000]$. While this power spectrum includes contributions from signals other than tSZ, we present numerous checks to show that the most challenging foreground signal, the cosmic infrared background (CIB) is much lower than the desired tSZ signal in the scales of interest in this work. The final tSZ power spectrum is measured at 9.3 σ with both the MV and CIB-min maps. Our results are consistent with those reported in other CMB surveys across the literature. Using the difference in the tSZ power spectrum from MV and CIB-min maps, we reconstruct the scale-dependent tSZ–CIB cross-correlation $\rho_{\ell}^{\text{tSZ} \times \text{CIB}}$, finding 3.1 σ evidence for a nonzero correlation coefficient that is positive on large scales and approaches zero for $\ell > 2500$.

This result represents the deepest tSZ maps ever produced and provides new constraints that can help refine astrophysical feedback mechanisms and models of the intracluster medium.

1. INTRODUCTION

Cosmic microwave background (CMB) photons free-streaming towards us from the surface of last scattering interact with structures at late times to produce the secondary anisotropies of the CMB. Consequently, the secondary anisotropies encode crucial information about structure formation in the Universe and are known to be excellent probes of both cosmology and astrophysics. The most dominant secondary CMB anisotropies include gravitational lensing (A. Blanchard & J. Schneider 1987; A. Lewis & A. Challinor 2006) and the Sunyaev-Zel'dovich (SZ) effect (R. Sunyaev & Y. Zel'dovich 1980; R. A. Sunyaev & Y. B. Zeldovich 1980), which has been detected at high significance in CMB maps alone and in cross-correlations of CMB maps with other cosmological surveys (B. A. Benson et al. 2004; M. E. Jones et al. 2005; K. M. Smith et al. 2007; Z. Staniszewski et al. 2009; S. Das et al. 2011; L. E. Bleem et al. 2015; Y. Omori et al. 2017; Planck Collaboration et al. 2020; M. S. Madhavacheril et al. 2024). The SZ effect can be further decomposed into the thermal-SZ (tSZ) effect, which is the inverse Compton scattering of CMB photons off free electrons in ionized regions (R. Sunyaev & Y. Zel'dovich 1980), and the kinematic-SZ (kSZ) effect, which is the Doppler boosting of CMB photons due to the bulk velocity of free electrons (R. A. Sunyaev & Y. B. Zeldovich 1980). In this work, we focus on the tSZ effect.

Over the past 20 years, the tSZ effect has emerged as a promising astrophysical and cosmological probe (E. Komatsu & U. Seljak 2002; N. Battaglia et al. 2012; Planck Collaboration et al. 2016a; S. Bocquet et al. 2024). The tSZ effect is now being routinely used by all major high-resolution CMB experiments to compile large samples of previously unknown galaxy clusters (Z. Staniszewski et al. 2009; L. E. Bleem et al. 2015; Planck Collaboration et al. 2016a; N. Huang et al. 2020; L. E. Bleem et al. 2020; M. Hilton et al. 2021; L. E. Bleem et al. 2024; K. Kornoelje et al. 2025; M. Archipley et al. 2026), including at high redshifts ($z \gtrsim 1.5$). Meanwhile, the power spectrum of the tSZ signal is also an excellent probe of structure formation (E. Komatsu & U. Seljak 2002; J. C. Hill & E. Pajer 2013; Planck Collaboration et al. 2016a; B. Horowitz & U. Seljak 2017, for example). To take advantage of this, groups have produced maps of the tSZ signal using data from the Atacama Cosmology Telescope (ACT, M. S. Madhavacheril et al. 2020; W. Coulton et al. 2024), the *Planck* satellite (Planck Collaboration et al. 2016b; J. Chandran et al. 2023),

and the South Pole Telescope (SPT, L. E. Bleem et al. 2022). Among other applications, these maps have been used to probe the gas physics of the Universe through signatures of cosmological shocks at cluster boundaries (E. J. Baxter & B. D. Sherwin 2021; D. Anbajagane et al. 2022), as well as through correlations of the tSZ signal with lensing and galaxy distributions (J. C. Hill & D. N. Spergel 2014; J. Sánchez et al. 2023; F. McCarthy & J. C. Hill 2024).

Recently, the tSZ effect has also been used extensively to study the impact of baryonic physics on structure formation, one of the leading candidates for the S_8 tension through small-scale suppression of the matter power spectrum (C. Preston et al. 2023, and references therein). Numerous groups have explored the impact of baryon physics on tSZ with the help of simulations (E. Moser et al. 2022; B. Hadzhiyska et al. 2023; S. Pandey et al. 2023; W. Elbers et al. 2025; I. G. McCarthy et al. 2025), while on the data side, work has mostly been limited to cross-correlations, for example, by cross-correlating tSZ maps with galaxy positions (E. Schaan et al. 2021; J. Sánchez et al. 2023; S. Das et al. 2023; R. H. Liu et al. 2025; N. Dalal et al. 2025) and comparing them to hydrodynamical simulations with different feedback prescriptions (I. G. McCarthy et al. 2014; J. Schaye et al. 2023).

The tSZ power spectrum is also sensitive to the baryonic feedback effect (I. G. McCarthy et al. 2014, for example). Baryonic feedback pushes gas out of the haloes and introduces a tilt in the tSZ power spectrum at arcminute ($\ell \gtrsim 3000$) scales (L. D. Shaw et al. 2010; I. G. McCarthy et al. 2014; W. Elbers et al. 2025). This effect could contribute to the strong suppression of the tSZ power spectrum reported by ACT (J. Dunkley et al. 2013; T. Louis et al. 2025) and SPT (E. M. George et al. 2015; C. L. Reichardt et al. 2021) at $\ell = 3000$ compared to a simple extrapolation of the large-scale measurements reported by *Planck* (Planck Collaboration et al. 2014a; B. Bolliet et al. 2018; H. Tanimura et al. 2022; J. Chandran et al. 2023). However, simulations suggest that resolving this discrepancy through baryonic feedback requires a significant and unrealistic amount of feedback (I. G. McCarthy et al. 2014, 2025). Another possible source of the discrepancy is unmodeled systematics in the measured power spectra, most likely related to the cosmic infrared background (CIB), and this remains an open question. The CIB is the diffuse signal component arising from dusty star-forming galaxies (DSFGs; M. P. Viero et al. 2019), which can partially fill

in the tSZ decrements at frequencies $\nu \leq 220$ GHz—the most sensitive bands for ACT and SPT—owing to the fact that both signals trace the underlying large-scale structure (J. Erler et al. 2018; V. L. Butler et al. 2022; K. Kornoelje et al. 2025). The small-scale measurements of the tSZ and kSZ power spectra by ACT and SPT (J. Dunkley et al. 2013; E. M. George et al. 2015; C. L. Reichardt et al. 2021) have thus far relied on assuming templates normalized at $\ell = 3000$ for both the signal components (tSZ/kSZ) and the undesired ones like the CIB. Since the CIB power, which has been known to be hard to model at sub-mm bands (M. P. Viero et al. 2019), dominates the total power spectrum at $\ell \geq 3000$ (see Fig. 2 of C. L. Reichardt et al. 2021, hereafter R21), any mismatch in the assumed templates can result in significant bias in the inferred SZ results, as demonstrated by S. Raghunathan & Y. Omori (2023, hereafter RO23).

In this work, we use data from SPT and *Herschel*-SPIRE to extract the full shape of the tSZ power spectrum in the multipole range $\ell \in [500, 5000]$, similar to the recent work by G. Efstathiou & F. McCarthy (2025), rather than a single $\ell = 3000$ data point as done in many of the previous works. Making use of the frequency dependence of different signal components, we combine the data from all frequency bands to derive the tSZ spectrum. While the measured total power spectrum includes contributions from undesired signals, we remove our best guess of this contamination using simulations. As mentioned above, the CIB is one of the undesired components that is difficult to model, and we perform a number of checks to ensure that any residual CIB contribution is small. The other components—CMB, kSZ¹, and radio—are comparatively straightforward to model. We also include systematic error budgets that account for uncertainties in modeling these components. Consequently, our reported measurement uncertainties incorporate both statistical errors and these additional systematic contributions. We estimate tSZ-only bandpowers in the multipole range $\ell \in [500, 5000]$. We also study and quantify the impact of source and cluster masking on the tSZ power spectrum.

Throughout this work, we use the D_ℓ convention in plots. D_ℓ is related to the angular power spectrum C_ℓ through $D_\ell = \frac{\ell(\ell+1)}{2\pi} C_\ell$.

¹ While the cross-correlation between kSZ and galaxies have been measured with high significance (J. C. Hill et al. 2016; S. Ferraro et al. 2016; A. Kusia et al. 2021), the auto-power spectrum of kSZ has not yet been measured with high precision. Nevertheless, we show that varying its amplitude has minimal impact on our results.

2. DATASETS AND METHODS

This work uses the same datasets as the kSZ trispectrum analysis by S. Raghunathan et al. (2024). We summarize the datasets here and refer the reader to the appendix of S. Raghunathan et al. (2024) for more details. The datasets for this analysis come from SPTpol (150 GHz, J. E. Austermann et al. 2012), SPT-3G (95, 150, and 220 GHz, B. A. Benson et al. 2014; A. N. Bender et al. 2018; J. A. Sobrin et al. 2022), and *Herschel*-SPIRE (600 and 857 GHz, G. L. Pilbratt et al. 2010; M. J. Griffin et al. 2010) surveys of a roughly 100 deg^2 region centered at right ascension (RA)= 352.5° (23h30m) and declination (Dec.)= -55° . The SPTpol observations were carried out between 2012 and 2016 while the SPT-3G observations are from the 2019 and 2020 seasons. The map depths at 95, 150, and 220 GHz correspond to 4.5, 3, and 16 $\mu\text{K}\text{-arcmin}$ respectively. To create the SPT maps, we filter the raw SPT time ordered data (TOD) and then bin them into flat sky maps in the Sanson-Flamsteed projection with a pixel resolution of $0.5'$ (K. K. Schaffer et al. 2011). The filtering and map-making procedures are similar to previous published SPT works (K. K. Schaffer et al. 2011; D. Dutcher et al. 2021, for example). The filtering scheme is employed to remove excess noise along the scan direction ℓ_x and to reduce aliasing when the TOD are binned into maps. After the maps are made, we cross-correlate the individual frequency maps with *Planck* to obtain absolute calibration factors.

2.1. Linear combination

We combine SPT and *Herschel*-SPIRE maps using the harmonic space linear combination (LC) technique (J.-F. Cardoso et al. 2008) to produce the final Compton- y maps. Before doing so, we deconvolve the experiment-dependent filter transfer function and the frequency-dependent beam window function from all the bands. For SPT, the beam used in the deconvolution is the version appropriate for a 2.7 K blackbody spectrum, and we refer to this as the “CMB” beam B_ℓ^{CMB} (N. Huang et al., in preparation). We also remove the signal from bright point sources detected in our maps. Specifically, we inpaint (A. Benoit-Lévy et al. 2013; S. Raghunathan et al. 2019) the location of both radio and dusty sources with flux above a certain threshold at 150 GHz (S_{150}) using the information from regions outside of the inpainting radius. The inpainting radius changes with the flux level of the sources and is $\sim 3'$ on average. We follow the inpainting procedure, rather than masking, to avoid artifacts during the ILC step. Our baseline results are with the inpainting threshold of $S_{150} = 2 \text{ mJy}$, chosen to significantly suppress the contamination from

point source signals, but we also repeat the procedure for other cases such as $S_{150} \in [6, 10, 20]$ mJy to quantify the change in tSZ power as a function of source masking. Due to masking, we lose roughly 18% of the total map area for the baseline case with $S_{150} = 2$ mJy, and 7%, 4%, and 2% for $S_{150} = 6, 10$, and 20 mJy masking thresholds.

The covariance matrix for the LC can be decomposed into two constituents: (a) experimental noise and (b) contribution from undesired signals like CMB, CIB, kSZ and radio galaxies. The noise covariance is calculated by randomly splitting our data into two sets M_A and M_B and calculating the 2D power spectrum of the half-difference map $(M_A - M_B)/2$. We repeat the procedure 100 times and take the average power spectrum to reduce the scatter in the noise covariance matrix. The covariance matrix of the undesired signals is calculated using the AGORA simulations (Y. Omori 2024). We note that any mismatch between the covariance in the simulations and that of the real data can lead to sub-optimal LC weights, but not to a bias in the recovered signal. However, in RO23 we showed that the residual levels remain essentially unchanged when the AGORA-based covariance used to compute the LC weights is replaced with a covariance model derived from SPT measurements (R21).

We produce four versions of the Compton- y maps: minimum-variance (MV), CMB-nulled (CMB-free), CIB-minimized (CIB-min) and Radio-minimized (Radio-min), using the LC and constrained-LC (cLC, M. Remazeilles et al. 2011) techniques. More specifically, as described in §2.3, we combine our observations into multiple map bundles and produce four versions of the Compton- y maps for each bundle. This bundling-approach is to avoid the noise bias when calculating the power spectrum and more details are provided in §2.3. The cLC approach allows minimizing the contribution from particular components. In cLC, the weights for each channel change compared to MV-LC based on the component being nulled or minimized. For this, we assume a spectral energy distribution (SED) to either remove or minimize CMB, CIB, and radio contamination (see Eq.(2) of RO23). We use the differential CMB temperature units $\Delta T_{\text{CMB}} = \Delta I_\nu \left[\frac{\partial B_\nu(T, \nu)}{\partial T} \Big|_{T_{\text{CMB}}} \right]^{-1}$ with respect to the average $T_{\text{CMB}} = 2.7255\text{K}$ where ν is the observed frequency (Planck Collaboration et al. 2014b). In these units, the SED for CMB is unity in all frequency bands. We model the frequency dependence of the radio sources using a power law with $\Delta I_\nu \propto \nu^{\alpha_{\text{radio}}}$ with $\alpha_{\text{radio}} = -0.76$ (R21). For CIB, we use a modified blackbody formalism of the form $\Delta I_\nu \propto \nu^{\beta_{\text{CIB}}} B_\nu(T_{\text{CIB}})$ where T_{CIB} is the temperature, β_{CIB} is the emissivity

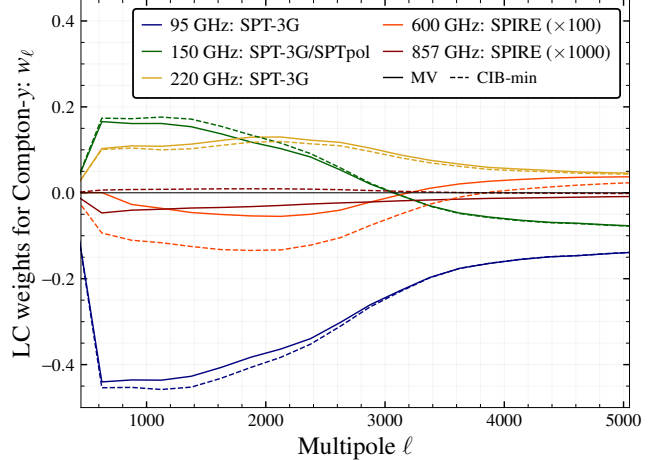


Figure 1. Azimuthally averaged LC weights for the MV and the CIB-min Compton- y maps. The solid (dashed) curves correspond to MV (CIB-min) maps. Since the weights are much smaller for the *Herschel*-SPIRE 600 (857) bands compared to the other bands, they have been multiplied by $\times 100$ ($\times 1000$) for clarity in this plot. As mentioned in the text, for the ease of analysis, we assume same weights for the 150 GHz channel from both SPT-3G and SPTpol.

index, and $B_\nu(T)$ is the *Planck* function. We use the grid-search procedure described in RO23 to determine the values of T_{CIB} and β_{CIB} that minimize the level of CIB contamination in the AGORA simulations over $\ell \in [500, 5000]$, given the noise properties of each frequency band. It is important to note that this method yields the lowest possible CIB residual for the chosen set of frequency bands and their associated noise levels; however, it does not guarantee that the resulting CIB residual is smaller than the tSZ signal itself. To account for this, as well as the fact that the SED used for the CIB-min map is based on AGORA, we perform numerous checks in §A.1.2 to ensure that any residual CIB contamination is much smaller than the desired tSZ signal.

Although the 150 GHz channels from SPT-3G and SPTpol have slightly different noise levels and beams, we assume identical LC weights for both channels to simplify the analysis. However, we deconvolve the appropriate beam B_ℓ^{CMB} from each of them. In Fig. 1, we show the LC weights for MV and CIB-min maps as solid and dashed curves, respectively.

The CMB-nulled and Radio-min maps, because of the relative weighting of the bands required to reduce the contribution from CMB and radio, are noisier than the others, and using simulations, we find that the residual CIB contribution in them is significantly higher than the expected level of tSZ on all scales. Consequently, we do not use them further in this analysis but they

are available to be downloaded as part of the associated data release.

2.2. Filter transfer function and beams

We capture the effect of filtering by calculating the transfer function (TF) using mock-observations of Gaussian simulations. The TF is the average ratio of the power spectrum of 250 mock-observed maps to the input spectrum used to generate the simulations. We calculate the TF in 2D as a function of both ℓ_x and ℓ_y to capture the anisotropic nature of the filtering. For *Herschel*-SPIRE, to remove excess noise on large scales, we high-pass filter the data at $|\ell_x| \lesssim 200$ and $|\ell_y| \lesssim 200$. The frequency-dependent beam window functions B_ℓ^ν for SPT are estimated using a combination of dedicated observations of planets and point sources in the CMB field data (D. Dutcher et al. 2021, Huang et al., in preparation). For reference, the SPT beams in the 95, 150, and 220 GHz bands can be approximated as Gaussians of width $\theta_{\text{FWHM}} = 1.^6, 1.^2, 1'$. We use Gaussian beam approximations for *Herschel*-SPIRE with $\theta_{\text{FWHM}} = 36.^6$ and $25.^2$ for the 600 and 857 GHz bands (M. P. Viero et al. 2019).

The variation of the experimental beam for different SEDs could be an important factor in the presence of foreground signals (S. Giardiello et al. 2025). We take this into account by modeling the main lobe of the SPT-3G beam for different SEDs to produce beams for multiple components: B_ℓ^{CIB} , B_ℓ^{Radio} , and B_ℓ^{tSZ} from an ongoing work (N. Huang et al., in preparation). The side-lobes are assumed to be frequency-independent. These component-dependent beams differ from the B_ℓ^{CMB} by: $\lesssim 2\%$ for B_ℓ^{Radio} ; $\lesssim 5\%$ for B_ℓ^{tSZ} ; and $\lesssim 10\%$ for B_ℓ^{CIB} in the desired range of scales $\ell \in [500, 5000]$. The variation is more for 220 GHz compared to 95/150 GHz.

2.3. Map bundles and cross-spectra

We follow previous works (R21, D. Dutcher et al. 2021; T. Louis et al. 2025; E. Camphuis et al. 2025) and calculate the tSZ power spectrum as the average of cross-power spectra between multiple Compton- y map bundles. Since the noise is different in each bundle, the cross spectra will not, on average, contain a contribution from the experimental noise. This ensures that we are insensitive to the mis-estimation of the noise power spectrum, which, in an auto-spectrum analysis, could lead to biases in the final tSZ power spectrum (G. Pontena et al. 2005; M. Tristram et al. 2005).

To this end, we randomly divide the SPT observations into 100 different bundles and take the inverse-variance weighted average of all the observations in each bundle. The bundles are chosen such that the noise is

roughly the same across all the different bundles. On the other hand, we only have two bundled maps M_A^{SPIRE} and M_B^{SPIRE} , rather than 100, for the *Herschel*-SPIRE 600/857 GHz bands. Consequently, we pick M_A^{SPIRE} (M_B^{SPIRE}) for all the even (odd) bundles in the LC step to create the Compton- y map. Before computing the power spectrum, we mask the inpainted locations in the Compton- y maps since the locations do not contain the true tSZ signal. Using simulations, we estimate that the mode-coupling that might arise due to masking is negligible and ignore it in the analysis. We compute the final binned tSZ power spectrum \hat{C}_b^{yy} in the range $\ell \in [500, 5000]$ in bins b of width $\Delta\ell = 500$ as:

$$\hat{C}_b^{\text{yy}} = \frac{1}{f_{\text{sky}}} \frac{1}{N} \sum_{\substack{i=\text{odd} \\ j=\text{even}}} (1 - \delta_{ij}) \sum_{\ell \in b} \frac{m_{\ell_i} m_{\ell_j}^*}{\Delta\ell} \quad (1)$$

where f_{sky} is the unmasked sky fraction, N is the total number of cross-spectra, m_ℓ is the Fourier transform of the Compton- y map m and the conditions ($i = \text{odd}$) and ($j = \text{even}$) ensure that we do not compute the cross-spectra of pairs of even bundles or pairs of odd bundles since such pairs contain the same *Herschel*-SPIRE 600/857 GHz data. The condition $(1 - \delta_{ij})$ ensures that we do not compute the auto-spectrum of any bundle, as it would be affected by the noise bias of that same bundle. In the subsequent sections we refer to the binned power spectrum \hat{C}_b^{yy} simply as C_ℓ^{yy} .

2.4. Simulations

We use the AGORA (Y. Omori 2024) extragalactic simulations and include experimental noise realizations either using one of the half-difference maps for SPT or using Gaussian realizations of the noise spectra for *Herschel*-SPIRE. We perform the exact same operations as done to the actual data before combining the simulations of the individual frequency bands using the LC step. These steps include filtering, convolving the simulations with the experimental beam, and inpainting. Note that we apply the component-dependent beams described in §2.2 to each of the foreground components in the simulations to properly mimic the real observations. The locations of the inpainted sources are different in simulations compared to data and are determined by combining the CIB and radio portions of AGORA at 150 GHz. We pick the locations of pixels above the masking threshold in the combined simulation and determine the masking radius based on the signal-to-noise (S/N) of sources with equivalent flux in data.

The AGORA simulation suite contains correlated multi-component sky signals, namely CIB, CMB, late-time kSZ, radio and tSZ. Since the correlation between

CIB, radio, and tSZ can be important for SZ inference (J. Dunkley et al. 2013, R21), and since we do not have robust high- S/N measurements of the cross-correlations, we cannot fully trust the CIB/radio/tSZ correlations in AGORA. Subsequently, we also randomly swap the location of the patch of each of these components to explicitly break the correlations between components in AGORA. We then inject different levels of scale-dependent correlations, as discussed in §3.4.1, to check the importance of these correlations. When doing so, we prefix each of the swapped components with `Uncorr-`. Finally, AGORA does not contain the contribution from the early-time reionization kSZ, and to include that, we generate Gaussian realizations with an underlying power spectrum corresponding to $C_\ell^{\text{kSZ,reion}} = \frac{1.5(2\pi)}{\ell(\ell+1)} \mu\text{K}^2$. Varying the level of reionization kSZ has no impact on our results.

The simulations are used for the following: computing the LC weights; determining the SED for CIB-min; obtaining the bandpower covariance matrix; performing systematic checks; and finally for estimating and removing the contribution of undesired signals (CIB, CMB, kSZ and radio) from the total measured spectrum to get the tSZ-only power spectrum. Since we only have a single realization of the AGORA simulation, we extract 100 non-overlapping 100 deg^2 patches corresponding to the size of our field (S. Raghunathan et al. 2024).

3. RESULTS

3.1. Compton- y maps and power spectrum measurement

Following the discussion in §2.3, we create a number of Compton- y maps from data and simulations as follows:

- **Data:** Two² Compton- y maps —MV and CIB-min—for all the hundred data map bundles. In total, we have $100 \text{ (bundles)} \times 2 \text{ (LC)} = 200$ maps.

In Fig. 2, we also show the MV Compton- y map reconstructed using the full dataset. The inset in top right shows the $6' \times 6'$ stack at the locations of clusters detected with $S/N \geq 20$ from K. Kornoelje et al. (2025). Note that we only use this full-coadd map for plotting; all power spectrum analyses are performed using cross-spectra of partial-depth maps.

- **Simulations:**

² As mentioned earlier in §2.1, we do not consider CMB-free and Radio-min maps for the power spectra estimation due to high levels of noise and CIB compared to the MV and CIB-min maps.

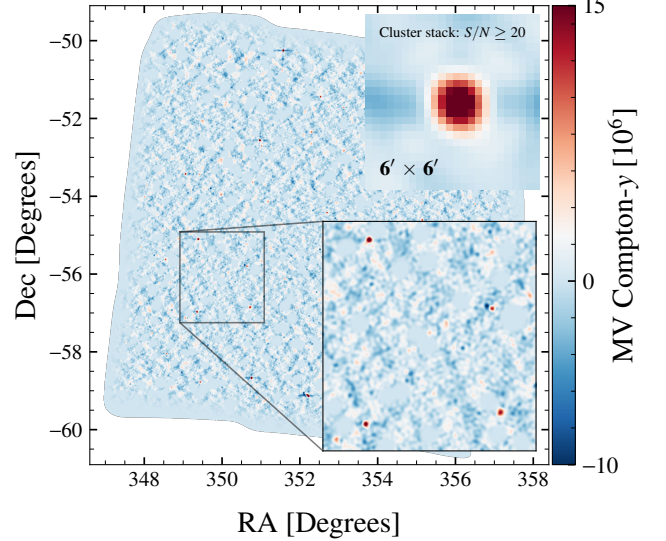


Figure 2. MV Compton- y map created using the full dataset. The increments (red dots) correspond to the cluster locations and the negative bowls around them correspond to the scan-direction filtering of the SPT maps, which we correct using TF during the power spectrum estimation stage. The inset panel in the top right shows the $6' \times 6'$ stack of clusters with $S/N \geq 20$ from K. Kornoelje et al. (2025).

- Set-A: For the systematic checks and to compute the expectation spectra from the undesired components, we use 25 AGORA simulations. For each simulation, to remove the noise bias in the power spectra, we create two sets of Compton- y maps with independent noise realizations. In total we have 25 (realizations) \times 2 (LC) \times 2 (bundles) = 100 maps. We find 25 realizations to be more than sufficient to reduce the sample variance since the templates converge after ~ 10 realizations.
- Set-B: To estimate the bandpower covariance matrix, we obtain the MV and CIB-min maps from 100 AGORA simulations that include experimental noise. Here, we have 100 (realizations) \times 2 (LC) = 200 maps. This covariance matrix—distinct from the one used to obtain the LC weights in §2.1—is used to capture both the measurement uncertainties and the correlations between adjacent ℓ bins of the tSZ power spectrum.

We compute the cross power spectra from the above data maps and Set-A simulations according to Eq.(1). To get the bandpower covariance matrix, we use the auto power spectra of the Set-B simulations. As described in §2.3, before computing the spectra, we mask the location of sources (which have been inpainted in the individual frequency maps) in the Compton- y maps.

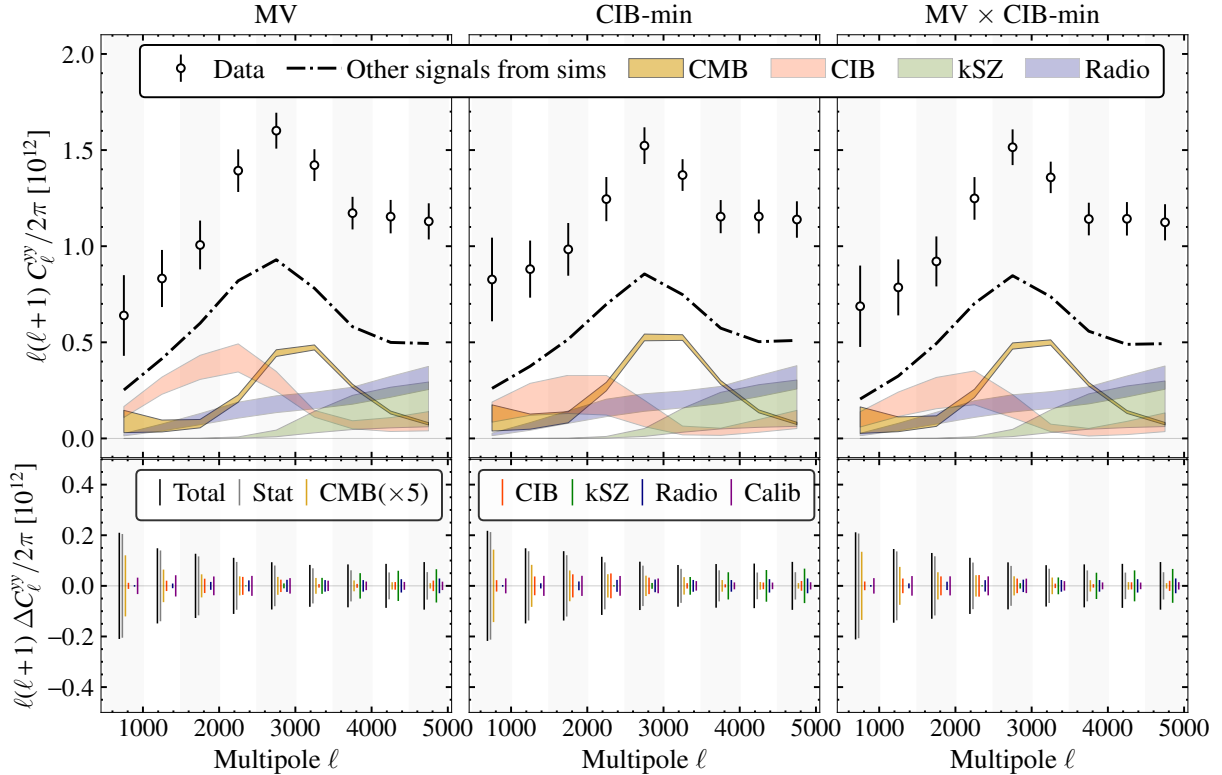


Figure 3. The total measured power spectra from data are shown as open circles in top panels for MV (left), CIB-min (middle), and the cross-spectrum between the two (right). The dash-dotted line corresponds to the expectation spectra of the undesired components with the individual contributions shown in different colors: CMB in yellow, CIB in red, kSZ in green and radio in blue. The dash-dotted curve does not have the tSZ contribution, so it is not expected to align with the data points. The bands correspond to the systematic scatter in each component (see text in §A for details). The error budgets (black) are presented in the bottom panels and have been decomposed into statistical (gray) and systematic errors from the undesired signals and calibration uncertainties (all other colors).

In the top panels of Fig. 3, we present the auto-power spectra for the MV (left) and CIB-min (middle) maps, and the cross-spectrum between the two maps (right). The open circles show the power spectra measured from data bundles. The black dash-dotted curves represent the expectation spectra for the undesired components—CMB, CIB, radio and kSZ—and have been averaged over 25 simulations. Note that these expectation spectra do not contain the tSZ signal and hence are not expected to align with the data shown as open circles. To be more specific, we compute the expectation spectra as the difference in power spectra obtained from (a) AGORA simulations containing CMB, Uncorr- CIB, Uncorr- radio, kSZ, tSZ and (b) tSZ-only AGORA simulations. As mentioned above, we break the correlations between tSZ and CIB/radio in simulations when calculating the expectation spectra and we discuss more about this in §3.4.1. We adopt this procedure rather than computing the expectation spectra from AGORA simulations that only contain CMB, CIB, radio and kSZ to ensure that the statistical properties of the simulations match the data

as closely as possible. To get the final tSZ-only spectra, we subtract the black dash-dotted curve from the data points; this step is discussed in more detail in the subsequent sections.

In the bottom panels of Fig. 3, we show the total band-power errors (black) that include both the statistical (gray) errors and the systematic errors (other colors), which are estimated as described in Appendix A. For ease of comparison, we have centered the errors on zero.

3.2. Bandpower errors and covariance matrix

We obtain the bandpower covariance matrix \mathbf{C}_{Stat} using the 100 Set-B AGORA simulations (see §3.1) for MV, CIB-min, and the cross-power spectrum between the two. Since the tSZ power spectrum is dominated by massive clusters that remain unmasked in this analysis, we expect the errors to be non-Gaussian leading to off-diagonal correlations in the covariance matrix. The non-Gaussian AGORA simulations should properly capture these correlations and also the sample variance from the tSZ signal. We also compute the systematic covari-

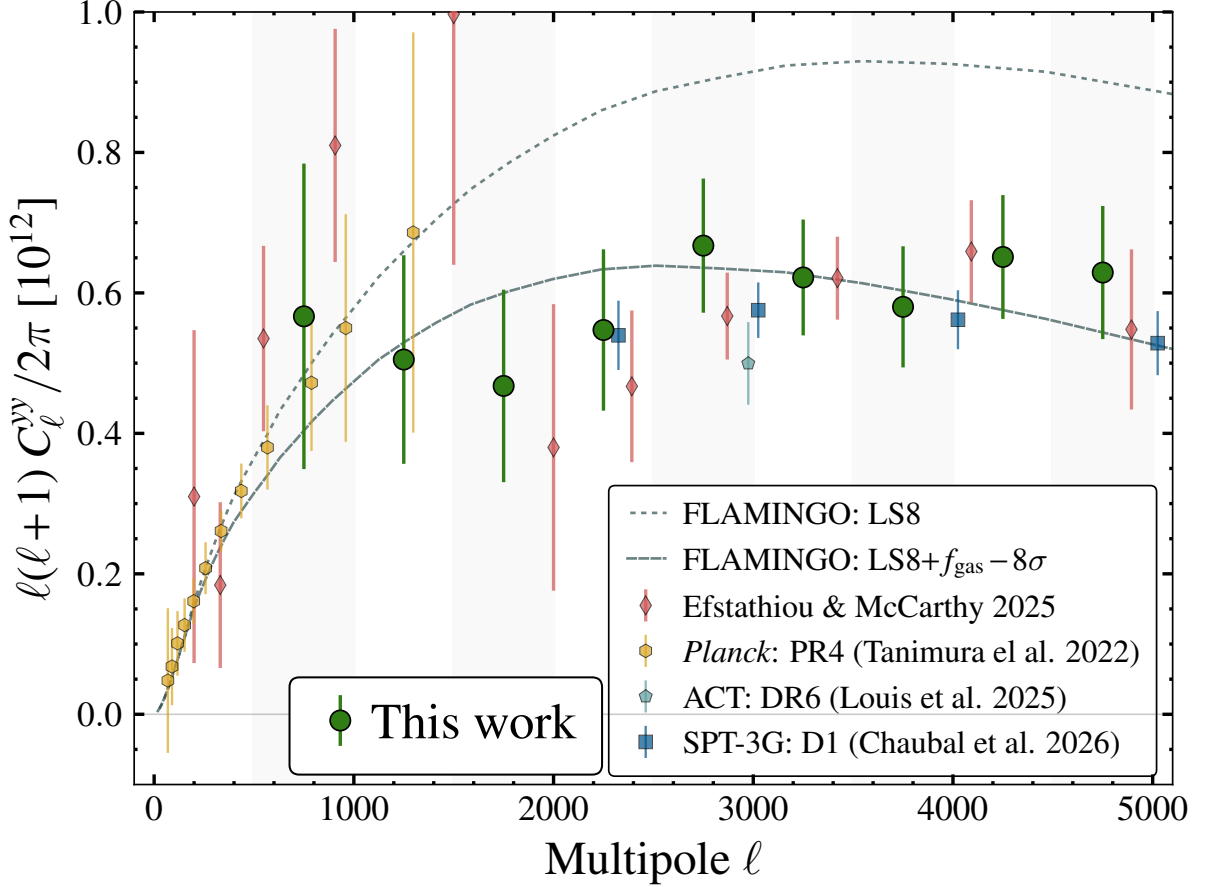


Figure 4. The tSZ power spectra measured at 9.3σ using the CIB-min maps is shown in green. The error bars include contributions from both statistical and systematic errors, and have significant off-diagonal correlations due to the non-Gaussian nature of the signals. We also show the results from *Planck* (PR4) as yellow hexagons; ACT (DR6) as a teal octagon; SPT-3G (D1) as blue squares; and a joint analysis of ACT, *Planck*, and SPT as red diamonds. While the results in this work are slightly higher than ACT at $\ell = 3000$ by 1σ , we find excellent agreement with *Planck* in the overlapping scales and also with the results from SPT-3G and G. Efstathiou & F. McCarthy (2025) over a wide range of scales. For reference, we also show the power spectra from versions of the FLAMINGO simulations as gray curves: the dotted curve is for the low S_8 (LS8) while the dashed curve corresponds to the model with high ($f_{\text{gas}} - 8\sigma$) AGN feedback.

ance matrix, \mathbf{C}_{Sys} , using the methods and results from Appendix A. Specifically, we compute \mathbf{C}_{Sys} for calibration errors, CMB, CIB, kSZ and radio using the scatter shown as bands in Fig. 3. The total covariance matrix is then

$$\begin{aligned} \mathbf{C}_{\text{Total}} = & \mathbf{C}_{\text{Stat}} + \mathbf{C}_{\text{Calib-Sys}} + \mathbf{C}_{\text{CMB-Sys}} + \\ & \mathbf{C}_{\text{CIB-Sys}} + \mathbf{C}_{\text{kSZ-Sys}} + \mathbf{C}_{\text{Rad-Sys}} \end{aligned} \quad (2)$$

and we show the square root of the diagonal of the total (black) and the individual components (Stat - gray; CMB - yellow; CIB - red; kSZ - green; Radio - blue; Calib - purple) in the lower panels of Fig. 3 for MV (left), CIB-min (middle), and MV \times CIB-min (right). For illustrative purposes, we enhance the systematic error due to CMB by $\times 5$ to demonstrate the relative size of error as a function of scale. We note that the large

scales are dominated by the statistical errors (mainly the sample variance) and the systematics errors become comparable to the statistical errors on small scales. The systematic errors are highly correlated between adjacent bins and this is taken into account in the covariance matrix.

3.3. tSZ power spectrum estimate

In this section, we report the final tSZ power spectrum estimates from this work and compare the results with the measurements reported by different surveys.

The green circles in Fig. 4 show the tSZ power spectrum measurements obtained here, derived from the cross-spectra of the 100 CIB-min Compton- y map bundles. As mentioned in §2.3, we do not compute the odd-odd or even-even cross-spectra since they have the

same *Herschel*-SPIRE splits and will be affected by the noise bias. The measurement significance is 9.3σ in the multipole range $\ell \in [500, 5000]$. The S/N drops by $20 - 27\%$ when reducing the small scale limit to $\ell_{\max} = 4000, 3500$, and 3000.

We adopt CIB-min as our fiducial estimate because the residual CIB bias arising from the tSZ–CIB cross-correlation has a minor impact on the large scales in both MV and MV \times CIB-min. In the next subsection (§3.4), we provide a detailed comparison of the tSZ estimates obtained from all three LC combinations (MV, CIB-min, and MV \times CIB-min), as well as discuss the scale-dependent reconstruction of tSZ \times CIB.

In Fig. 4, we also show measurements reported by different groups in the literature: *Planck* (PR4) as yellow hexagons (H. Tanimura et al. 2022); ACT (DR6) as a teal octagon (T. Louis et al. 2025); and the measurement from a joint analysis of *Planck*, ACT, and SPT data as red diamonds (G. Efstathiou & F. McCarthy 2025). We also show the recent results from SPT-3G (D1) (P. Chaubal et al. 2026) as blue squares. The contribution from other components are either removed or taken into account using multi-component fits in all these works. Our results are higher than the ACT measurements at $\ell = 3000$ by $\sim 1\sigma$. However, we find excellent agreement with *Planck* data in the overlapping scales $\ell \in [500, 1100]$ and also with SPT-3G (D1) at $\ell \geq 2000$. Our results are also in good agreement with the results of G. Efstathiou & F. McCarthy (2025), over a wide range of scales, particularly at $\ell \geq 2000$.

For reference, we also plot the tSZ power spectrum from FLAMINGO simulations (Fig. 6 of I. G. McCarthy et al. 2025) as gray curves. We emphasize that these curves are not fits to our measurements but are shown solely for illustrative purposes. As inferred by I. G. McCarthy et al. (2025), the LS8 cosmology model (dotted gray curve) with a lower value of $S_8 = 0.766$ but with the fiducial Active Galactic Nucleus (AGN) feedback model, derived based on joint analysis of galaxy clustering and weak lensing measurements, is a better fit to the large-scale measurements of the tSZ power spectrum compared to the fiducial value of $S_8 = 0.833$ from *Planck* CMB measurements. However, this model over predicts the tSZ power spectrum on small-scales compared to the measurements as can be seen in the figure and also shown by I. G. McCarthy et al. (2025); G. Efstathiou & F. McCarthy (2025). On the other hand, a tuned LS8 model with a high level (a model with feedback higher than the fiducial level by eight times the calibration uncertainty in the simulation) of feedback, LS8+ $f_{\text{gas}} - 8\sigma$, shown as the gray dashed curve, matches our results better. Note that both the models converge on large-scales,

matching the *Planck* measurements, since those scales are dominated by massive, low-redshift clusters, which are less affected by feedback processes (I. G. McCarthy et al. 2025).

3.4. tSZ power spectrum from different LC techniques and tSZ \times CIB reconstruction

In §3.3, we presented the tSZ power spectrum results derived from the CIB-min technique and compared it with other works from the literature. In the left panel of Fig. 5, we show and compare the results from different LC combinations: MV (red squares), CIB-min (green circles), and the cross-spectrum of the two (yellow diamonds). These are obtained by subtracting the expectation spectra of the undesired signals (shown as the black dash dotted curve in Fig. 3) from the total power spectra (open circles in Fig. 3). The systematic errors in the expectation spectra, described above, are taken into account in the errors. As mentioned in the main text, the adjacent bins are correlated due to the non-Gaussian nature of the covariance. We measure the tSZ power spectra in the multipole range $\ell \in [500, 5000]$ at 9.4σ with MV, 9.3σ with CIB-min, and 9.4σ using the MV \times CIB-min cross spectrum. There is an excellent agreement between all three spectra at scales $\ell \gtrsim 2500$. At large scales, CIB-min data points in green are slightly higher in the range $\ell \in [1500, 2500]$. This is due to the partial cancellation of the tSZ signal and the residual CIB caused by non-zero tSZ \times CIB, which impacts the MV estimate more. In this work, we reconstruct the scale-dependent tSZ \times CIB, since, beyond the challenges of accurately modeling the CIB, the tSZ \times CIB correlation itself remains a major obstacle to extracting robust information from both the kSZ and tSZ signals (R21; RO23).

To build intuition about the impact of tSZ \times CIB on the reconstructed tSZ power spectra, we present the simulation results, averaged over 25 simulations, in the right panels of Fig. 5. In the top right panel, we show results that include all the components from AGORA simulations but after explicitly removing the correlation between tSZ and CIB, (i.e.) CMB + kSZ + tSZ + Uncorr-CIB + Uncorr-radio. In this case, the recovered tSZ power spectrum estimates for all three cases match the input tSZ, shown as the solid gray curve. This further demonstrates that our pipeline yields unbiased results. In contrast, when tSZ \times CIB is present (bottom right panel), the residual CIB contributions partially cancel the tSZ signal, resulting in a biased estimate. This bias is most pronounced for MV and somewhat reduced for MV \times CIB-min, while the CIB-min method remains unbiased. The trend in tSZ amplitude among

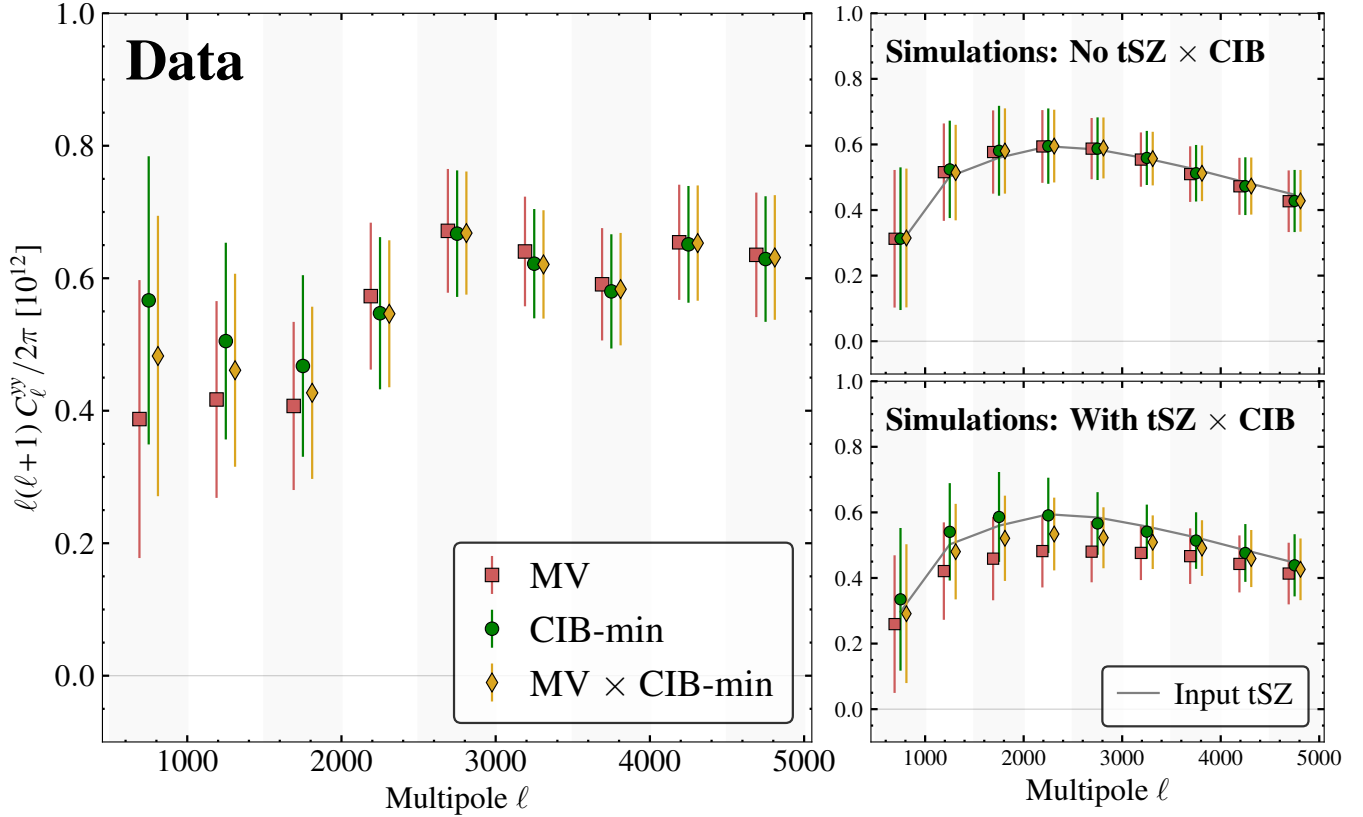


Figure 5. Reconstructed tSZ power spectra measured from data (left) and simulations (right): MV (red squares), CIB-min (green circles), and their cross-spectrum (yellow diamonds). *Left panel:* In data, the tSZ power spectrum is measured at $\sim 9.3\sigma$ in all the three cases. At $\ell \gtrsim 2500$, we find excellent agreement between all three spectra. The differences at lower multipoles are due to the different levels of tSZ \times CIB, which results in a partial cancellation of the recovered tSZ signal. *Right panels:* The input tSZ power spectrum in simulations is shown as the gray curve. The top right panel corresponds to AGORA simulations with all the components but after explicitly removing the tSZ \times CIB using (CMB + kSZ + tSZ + Uncorr-CIB + Uncorr-radio). In the absence of tSZ \times CIB, all of the estimators return unbiased results. The bottom right panel contains tSZ \times CIB, and in this case, we find the MV estimate to be biased low at large scales. The CIB-min remains unbiased and MV \times CIB-min lies in between the two. The simulations results are obtained after averaging over 25 realizations. This trend is similar between data and simulations, although unlike in the empirical data, the simulations show that MV remains biased even at small scales. This is due to the differences in tSZ \times CIB between data and simulations. The bottom right panel is provided solely for illustration to build intuition about how the tSZ \times CIB can bias the tSZ power spectrum, and we emphasize that we do not rely on tSZ \times CIB in simulations for any part of our analysis.

the different LC estimates is similar in the data (left) and the simulations (bottom right). However, we note that in the simulations, the MV estimate differs from the others over all relevant scales, while in the data the three LC estimates agree at $\ell \gtrsim 2500$. This difference between the data and simulations arises from differences in the tSZ \times CIB contribution. Since the scale dependence of the tSZ \times CIB has not been detected at high significance to date, this correlation is not properly calibrated in the simulations. Consequently, we do not use tSZ \times CIB in the simulations in our analysis.

3.4.1. Reconstructing the cross-correlation between tSZ and CIB

Based on the data and simulation results shown in Fig. 5, we attribute the differences among the reconstructed tSZ power spectra from the three LC estimates to tSZ \times CIB, and we use these differences to reconstruct the tSZ \times CIB cross-correlation. To this end, we compute the difference spectrum between two tSZ power spectrum estimates X and Y

$$\Delta C_{\ell_{XY}}^{yy} = C_{\ell_X}^{yy} - C_{\ell_Y}^{yy}, \quad (3)$$

where X, Y correspond to the power spectrum of different LC estimates. Specifically, they correspond to auto-spectrum $\alpha\alpha$ or the cross-spectrum $\alpha\beta$ of the LC

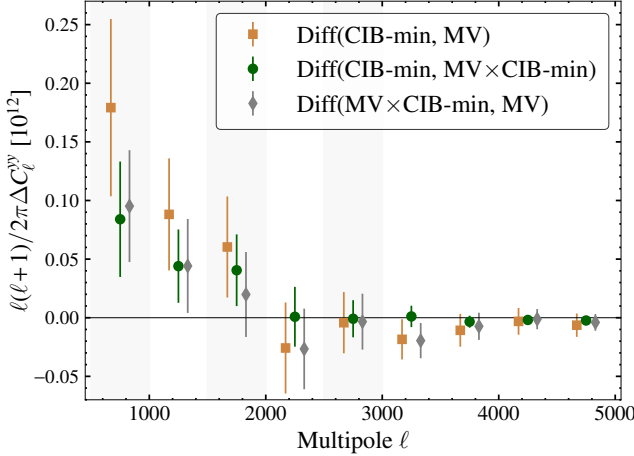


Figure 6. The difference spectrum $\Delta C_{\ell XY}^{yy}$ computed from different LC combinations are shown. The difference spectrum should be consistent with zero in the absence of any bias and we attribute the differences to the residual CIB bias arising due to tSZ \times CIB. The error bars are computed using the square root of the diagonal of the covariance matrix of the difference spectrum in Eq.(4). As is the case for C_{ℓ}^{yy} , the adjacent ℓ bins are highly correlated.

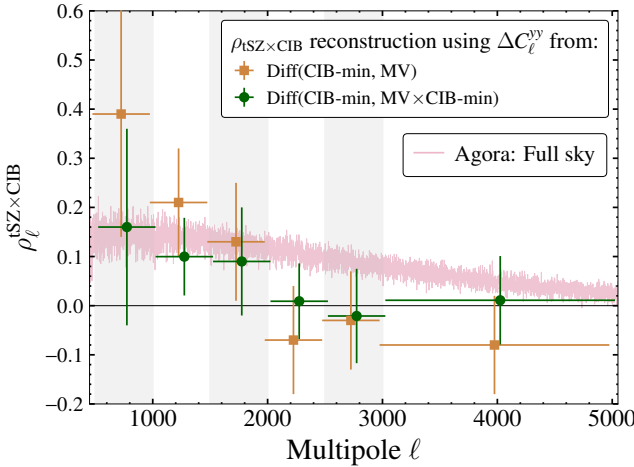


Figure 7. Reconstructed scale-dependent $\rho_{\ell}^{tSZ \times CIB}$ using the difference spectrum from two LC combinations: (CIB-min, MV) as yellow squares and (CIB-min, MV \times CIB-min) as green circles. Combining all the bins, which are highly correlated, we find 3.1σ and 2σ for a non-zero $\rho_{\ell}^{tSZ \times CIB}$ from the two cases. For illustrative purposes, we additionally present the $\rho_{\ell}^{tSZ \times CIB}$ inferred from the AGORA simulations, shown in pink, although it is not used in any part of our analysis. The full corner plot is presented in Fig. 8.

estimates with $\alpha, \beta \in [\text{MV}, \text{CIB-min}]$. The covariance of this difference spectrum is given as

$$\mathbf{C}_{XY} = \mathbf{C}_{\alpha\alpha} + \mathbf{C}_{\beta\beta} - 2\mathbf{C}_{\alpha\beta}. \quad (4)$$

We show $\Delta C_{\ell XY}^{yy}$ computed for different combinations in Fig. 6: green circles are for $(X, Y) = (\text{CIB-min}, \text{MV} \times \text{CIB-min})$; yellow squares are for $(X, Y) = (\text{CIB-min}, \text{MV})$; and gray diamonds are for $(X, Y) = (\text{MV} \times \text{CIB-min}, \text{MV})$. In the absence of any bias, $\Delta C_{\ell XY}^{yy}$ is expected to be consistent with a null spectrum within the errors. We attribute the bias to the cancellation of the tSZ signal by the residual CIB present in the Compton- y maps arising due to tSZ \times CIB and use this information to study $\rho_{\ell}^{tSZ \times CIB}$.

We reconstruct $\rho_{\ell}^{tSZ \times CIB}$ in multiple ℓ bins to understand how the cross-correlation changes with scales. We adopt six bins in our fiducial setup: (a) five bins with $\Delta\ell = 500$ for $\ell \in [500, 3000]$ and (b) a single large bin for $\ell \in [3000, 5000]$. The binning choice is also highlighted as light gray shaded regions in Fig. 6. There are negligible changes to the results when we use the same binning used for C_{ℓ}^{yy} with $\Delta\ell = 500$ for $\ell \in [500, 5000]$. This is because the difference spectra $\Delta C_{\ell XY}^{yy}$ are consistent with zero at $\ell \gtrsim 2500$. The parameter estimation is carried out using a Markov Chain Monte Carlo (MCMC) framework, utilizing the Code for BAYesian Analysis (cobaya³, J. Torrado & A. Lewis 2021) to sample the posterior distributions with the Metropolis-Hastings sampler. The chains are analyzed using the GetDist⁴ package and we set the Gelman-Rubin statistic $R - 1 = 0.01$ implemented in cobaya based on A. Lewis (2013) to attain the chain convergence.

We perform the fitting in power spectrum space (using the beam and transfer function deconvolved results). We compare the data vectors $\Delta C_{\ell XY}^{yy}$ obtained from the differences of the LC combinations to models computed for the corresponding LC combinations as follows. Given the power spectra of tSZ C_{ℓ}^{tSZ} and CIB C_{ℓ}^{CIB} in two frequency bands ν_1 and ν_2 , we define the tSZ \times CIB cross-spectrum $C_{\ell_{\nu_1 \nu_2}}^{tSZ \times CIB}$ using a scale-dependent correlation coefficient $\rho_{\ell}^{tSZ \times CIB}$ as

$$C_{\ell_{\nu_1 \nu_2}}^{tSZ \times CIB} = -\rho_{\ell}^{tSZ \times CIB} \sqrt{C_{\ell_{\nu_1}}^{CIB} C_{\ell_{\nu_2}}^{tSZ}} \quad (5)$$

where ν_1, ν_2 correspond to one of the six frequency bands from the SPT-3G, SPTpol, and *Herschel*-SPIRE surveys.

In Eq.(5), the CIB power spectra for different bands come from AGORA simulations. For the tSZ power spectra, we follow two approaches. In the first approach, we use the Compton- y power spectrum derived from CIB-min LC estimates (green points in Fig. 4) and multiply

³ <https://cobaya.readthedocs.io/en/latest/>

⁴ <https://getdist.readthedocs.io/en/latest/index.html>

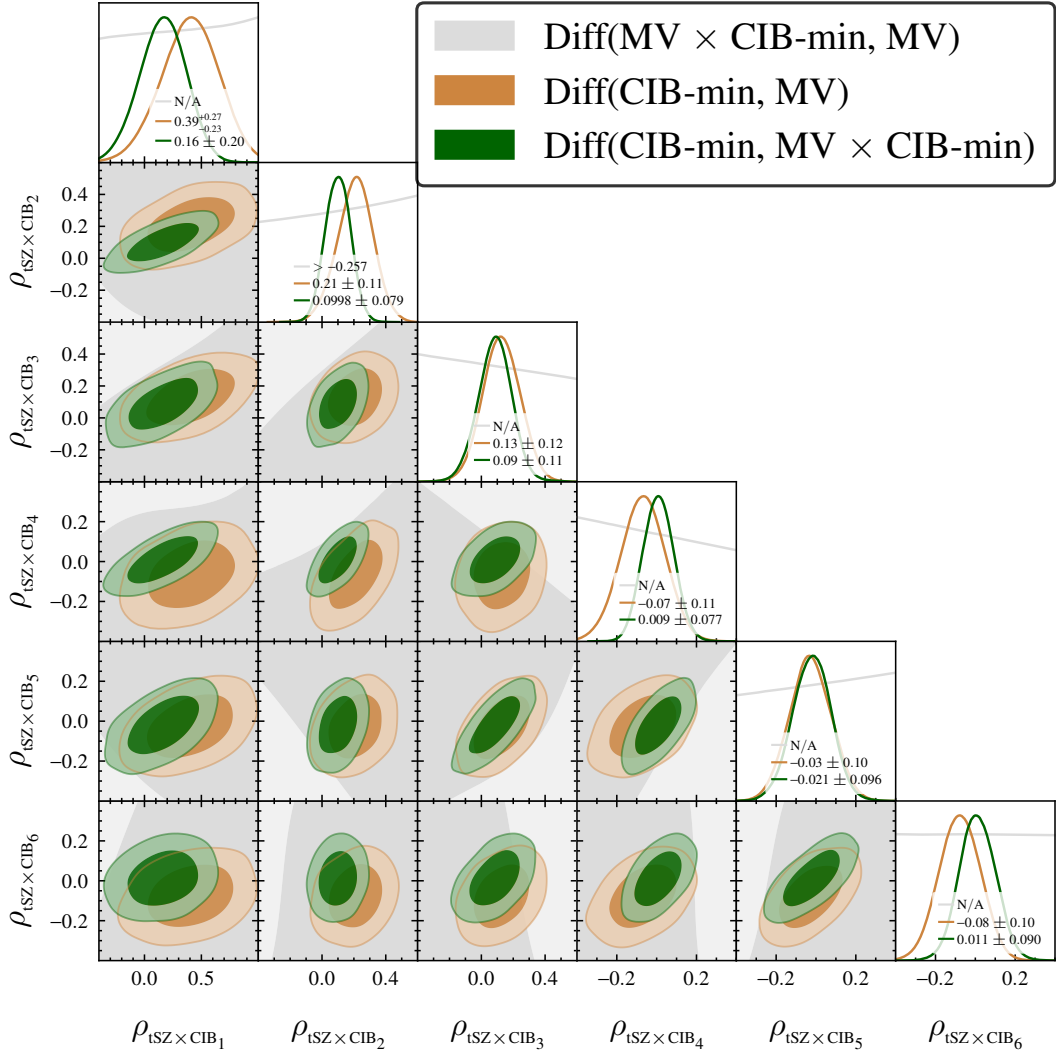


Figure 8. Full corner plot showing the correlations between $\rho_{\ell}^{\text{tSZ} \times \text{CIB}}$ in the six bins shown in Fig. 7. The colors follow the same scheme as Fig. 6 and Fig. 7. For completeness, we also include in gray the results from the difference test of $(\text{MV} \times \text{CIB-min}, \text{MV})$; however, this test provides no additional constraining power.

the spectrum by the tSZ frequency dependence to get to the ΔT_{CMB} units in μK . In the second approach, we use the tSZ power spectra from AGORA simulations. The first approach is appealing because it is independent of amplitude and shape differences between the true tSZ power spectrum and the simulations. However, this approach implicitly assumes that the bias due to $\text{tSZ} \times \text{CIB}$ is zero in the CIB-min estimate. The second approach, on the other hand, is immune to the bias from $\text{tSZ} \times \text{CIB}$, but it can be affected by mismatches between the true underlying tSZ power spectrum and the simulations. Thus, the two approaches are complementary, and our results change only minimally between the two cases. Note that in both approaches, we do not use the $\text{tSZ} \times \text{CIB}$ in simulations and inject our own scale-dependent correlation based on Eq.(5).

We apply the LC weights for two different Compton- y estimates $w_{\ell_{\alpha}}$ and $w_{\ell_{\beta}}$ to $C_{\ell_{\nu_1 \nu_2}}^{\text{tSZ} \times \text{CIB}}$ and obtain the final LCed estimate $C_{\ell_{\alpha \beta}}^{\text{tSZ} \times \text{CIB}}$ as given below:

$$C_{\ell_{\alpha \beta}}^{\text{tSZ} \times \text{CIB}} = w_{\ell_{\alpha}} \mathbf{C}_{\ell}^{\text{tSZ} \times \text{CIB}} w_{\ell_{\beta}}^{\dagger}. \quad (6)$$

Finally, we compute the model vector as

$$\Delta C_{\ell_{X,Y,\text{model}}}^{yy} = 2(C_{\ell_X}^{\text{tSZ} \times \text{CIB}} - C_{\ell_Y}^{\text{tSZ} \times \text{CIB}}). \quad (7)$$

To reduce scatter from a single simulation, we apply the above operations to 25 simulations and adopt the resulting average as our final model vector.

In our baseline case, we have six free parameters corresponding to $\rho_{\ell_i}^{\text{tSZ} \times \text{CIB}}$ in the six ℓ_i bins described above. We assume uniform priors $\mathcal{U}(-1, 1)$ for all bins. We present the results in Fig. 7 which shows the best-fit

results for $(X, Y) = (\text{MV}, \text{CIB-min})$ as yellow squares and $(X, Y) = (\text{CIB-min}, \text{MV} \times \text{CIB-min})$ as green circles. Since the tSZ \times CIB partially cancels in $(X, Y) = (\text{MV} \times \text{CIB-min}, \text{MV})$, that test is not as constraining as the other two tests, as shown in Fig. 8. The cross-correlation coefficient is non-zero on large scales ($\ell < 2500$), but it decreases and approaches zero at smaller scales. Combining all six bins, we obtain 3.1σ and 2σ evidence for non-zero $\rho_\ell^{\text{tSZ} \times \text{CIB}}$ for the two cases presented above, and they both agree well with each other. For reference, we also show the $\rho_\ell^{\text{tSZ} \times \text{CIB}}$ computed from AGORA simulations as the pink curve. We do not use AGORA $\rho_\ell^{\text{tSZ} \times \text{CIB}}$ in any part of our analysis. These results correspond to approach (A) where the tSZ power spectra used for modeling $C_{\ell_{\nu_1 \nu_2}}^{\text{tSZ} \times \text{CIB}}$ are obtained from CIB-min results. We find negligible impact on the results when we switched to the tSZ power spectrum from AGORA simulations (Approach B). We also checked the impact of beam uncertainties (§A.3) and also find them to be negligible.

The full corner plot is shown in Fig. 8 along with the best-fit values and uncertainties quoted in the 1d posteriors along the diagonal. We do not find the LC combination $(X, Y) = (\text{MV}, \text{MV} \times \text{CIB-min})$, shown in gray, to be highly constraining and hence do not add those results in Fig. 7. Although the green contours appear tighter in Fig. 8, the values of $\rho_\ell^{\text{tSZ} \times \text{CIB}}$ in adjacent bins are more strongly correlated than in the case of the yellow contours. This is intuitively reasonable, since the CIB-min estimates enter into both X and Y in that case.

3.5. Impact of cluster masking on the tSZ power spectrum

Several studies have utilized both observational data (E. M. George et al. 2015; J. Hernandez et al. 2023) and simulations (e.g., G. P. Holder et al. 2007; I. G. McCarthy et al. 2014; S. Raghunathan 2022; B. Hadzhiyska et al. 2023) to investigate how the tSZ power spectrum relates to cluster mass, redshift, and environment, with the ultimate goal of accurately modeling the gas physics of the intracluster medium (ICM).

In this section, we quantify the changes in the tSZ power spectrum resulting from masking the detected clusters in the maps. To this end, we mask the locations of 285 (63) clusters detected at $S/N \geq 5$ ($S/N \geq 10$) from the K. Kornoelje et al. (2025) catalog. These roughly correspond to clusters with $M_{500c} \sim 1.5$ (2.5) $\times 10^{14} M_\odot$ at a median redshift $z \approx 0.7$ (S. Raghunathan 2022; K. Kornoelje et al. 2025). Similar to source masking, the cluster masking radius also changes based on the detection significance and is roughly between $3' - 7'$.

The results are shown in Fig. 9: baseline results where the clusters remain unmasked are shown as red circles, while the blue hexagons (yellow squares) correspond to the results after removing the contribution from clusters with $S/N \geq 5$ ($S/N \geq 10$). The top panels show the power spectrum for masked and unmasked cases, and in the bottom panels we present the ratio of masked over the unmasked data points. The two masking schemes result in a suppression of the tSZ power spectrum by $\times 1.8$ and $\times 1.5$ at $\ell = 3000$. The power suppression due to cluster masking is roughly constant at $\ell > 1000$. However, in the first bin, the power suppression due to cluster masking is much smaller ($\lesssim 10\%$), due to large-scale SPT filtering. The decrease in power at small scales is slightly lower than those reported by S. Raghunathan (2022) who predicted roughly $\times 2$ reduction of the power (after accounting for the differences in the noise levels between the two studies). This discrepancy may stem from differences between the true cluster profiles and the generalized Navarro–Frenk–White (gNFW; J. F. Navarro et al. 1996, D. Nagai et al. 2007) profile assumed in S. Raghunathan (2022), as well as from large-scale SPT filtering and astrophysical feedback effects that are not accounted for in that analysis. We do not attempt to decompose the tSZ power from multiple cluster mass and redshift bins (as done by J. Hernandez et al. 2023) and leave such an analysis, both with the tSZ-selected clusters and the external catalogs from optical/X-ray observations, to future work. This can also help us understand the changes to the tilt of the spectra for different levels of cluster-masking which can give insights into the mass/redshift evolution of the gas physics of clusters.

3.6. Effects of source masking

Now we turn to the impact of source masking on the tSZ power spectrum. As a reminder, in our baseline analysis, we have removed the contribution of sources with flux $S_{150} \geq 2$ mJy. Here, we repeat the analysis after changing the masking threshold to the following: $S_{150} \in [6, 10, 20]$ mJy. Although we do not differentiate between radio (synchrotron) and dusty sources, this exercise should primarily probe the correlation between the tSZ and bright ($S_{150} \in [2, 20]$ mJy) radio galaxies. This is because the brightest unmasked radio sources dominate the radio Poisson power in typical CMB observation bands (95/150 GHz), while the CIB power primarily originates from faint sources below the masking threshold (R21).

We rerun the entire pipeline on both data and simulations (CMB + kSZ + tSZ + Uncorr-CIB + Uncorr-radio) to reconstruct the tSZ map for different

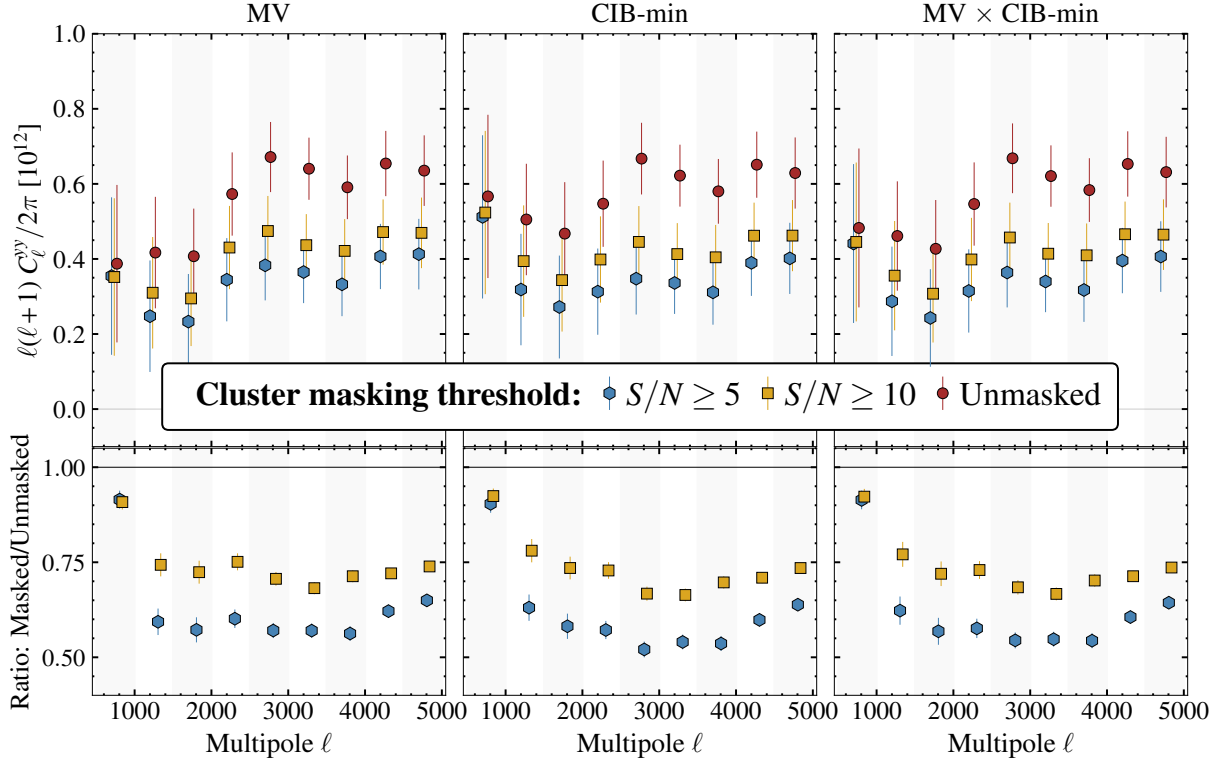


Figure 9. Changes to the measured tSZ power spectrum when clusters are masked in the analysis. The top panels show the actual values while the bottom panels show the ratio for different LC schemes. Red circles correspond to the baseline unmasked case while the blue hexagons (yellow squares) are after masking clusters detected with $S/N \geq 5$ ($S/N \geq 10$) from the SPT cluster catalog (K. Kornelje et al. 2025). The tSZ power reduces by $\times 1.8$ and $\times 1.5$ at $\ell = 3000$ for the two masking schemes.

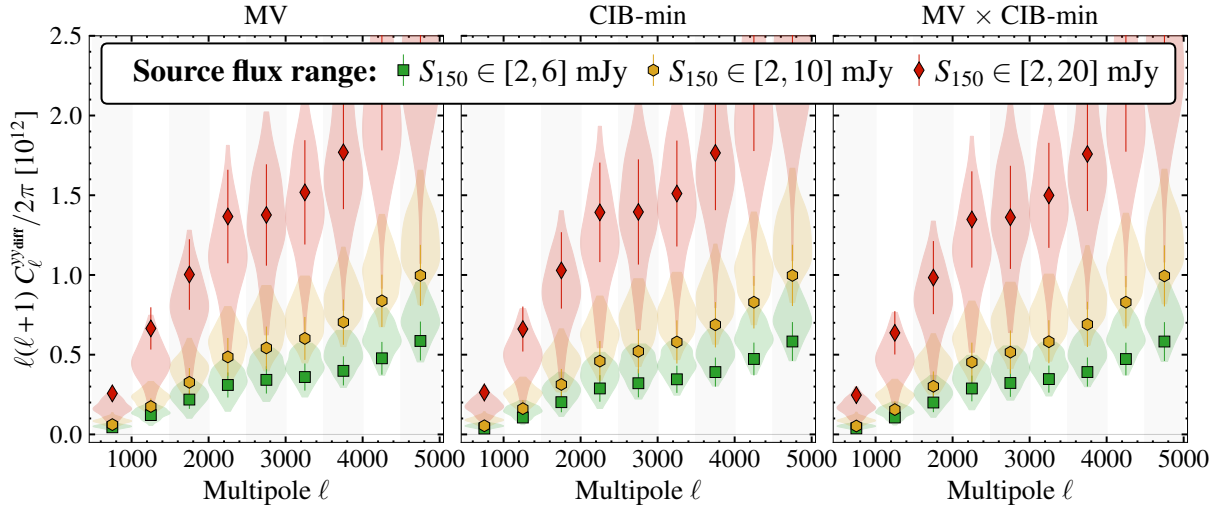


Figure 10. Power spectra of the difference maps $C_\ell^{yy,\text{diff}}$ computed by subtracting the baseline case of $S_{150} = 2$ mJy from the maps made with other source masking schemes: $S_{150} = 6$ mJy (green), $S_{150} = 10$ mJy (yellow), and $S_{150} = 20$ mJy (red). The violins show the scatter from simulations which include both the statistical and the systematic errors from radio sources. The simulations used are CMB + kSZ + tSZ + **Uncorr**-CIB + **Uncorr**-radio, and does not contain correlation between tSZ and bright sources. The observed differences are consistent within the errors, which increase significantly with the masking threshold due to the residual radio power, and we do not observe a significant correlation between tSZ and bright point sources detected in our survey footprint.

($S_{150} \in [6, 10, 20]$ mJy) point source masking schemes. Next, we subtract the baseline tSZ map ($S_{150} = 2$ mJy masking) from each of the above maps and compute the power spectrum of this difference map which we represent as $C_\ell^{yy\text{diff}}$. The signals in the unmasked regions are removed in the difference maps, so we are only sensitive to signals within the point source mask regions. This contribution is dominated by the signal from unmasked point sources, along with non-zero contributions from the CMB, kSZ, and tSZ signals at the source locations, as well as correlations among these components.

We present the results in Fig. 10: green squares, yellow hexagons, and red diamonds correspond to thresholds of $S_{150} \in [6, 10, 20]$ mJy used in the difference maps. A first observation is that the signal in the difference maps $C_\ell^{yy\text{diff}}$ is substantially larger than in the baseline-masking case shown in Fig. 4, particularly for the 10 and 20 mJy masking thresholds, and is dominated by point sources. This illustrates the rationale behind our choice of applying a masking threshold of $S_{150} = 2$ mJy for the baseline case. The violins in the figure show the scatter in the simulations which includes both the statistical errors and also the systematic error from the uncorrelated radio sources as described in §A. We quantify the agreement between the data and the simulations (which do not include the correlation between the tSZ signal and bright point sources) by computing the χ^2_{null} for each case. We define the p -value as the fraction of simulations with χ^2_{null} larger than that of the data, and we find that these values lie in the range 0.1–0.9 across all cases. Thus the observed changes are fully consistent with the scatter expected from the simulations, indicating no significant correlations between tSZ and the bright radio sources in our field.

4. CONCLUSION

In this work, we presented the full shape of the tSZ power spectrum in the range $\ell \in [500, 5000]$ reconstructed by combining data from the SPT and *Herschel*-SPIRE datasets using linear combination techniques. After removing the expected contribution from undesired residual signals, namely the CMB, CIB, kSZ and radio, we have measured the tSZ power spectrum at 9.3σ . We presented numerous checks and quantified the systematic errors due to the assumptions about the residual signals. The results are consistent with *Planck* measurements (H. Tanimura et al. 2022) on the overlapping scales $\ell \in [500, 1100]$, as well as with the recent results from G. Efstathiou & F. McCarthy (2025) and SPT-3G (P. Chaubal et al. 2026) over a wide range of scales.

We used the difference in the tSZ power spectrum estimates from different combinations of the LC methods to derive the scale-dependent cross-correlation between tSZ and CIB $\rho_\ell^{\text{tSZ} \times \text{CIB}}$. We found the correlation coefficient to be ~ 0.2 on large scales but the correlation drops towards zero at $\ell > 2500$. The evidence for a non-zero $\rho_\ell^{\text{tSZ} \times \text{CIB}}$ is at the 3.1σ level.

We also studied the impact of source and cluster masking on the tSZ power spectrum. The tSZ power spectrum does not change significantly with different source masking thresholds implying weak tSZ \times radio correlation for the bright $S_{150} \geq 2$ mJy sources in our survey. Masking the detected clusters results in a suppression of the tSZ power, matching with the expectations. When we masked clusters detected with $S/N \geq 5$ (K. Kornoelje et al. 2025), we found that the tSZ power at $\ell = 3000$ reduced by $\times 1.8$. The ratio remains roughly constant at $\ell > 1000$ although the power suppression due to cluster masking in the first bin is much smaller ($\lesssim 10\%$), due to large-scale filtering in SPT maps.

To our knowledge, the maps produced in this work represent the deepest tSZ maps ever produced. The analysis pipeline and the tools used in this work are also currently being applied to other datasets within the SPT-3G collaboration to produce deep tSZ maps over much larger footprints covered by the SPT-3G survey (K. Prabhu et al. 2024).

The tSZ maps and the power spectrum, particularly at small scales, as well as the characterization of tSZ \times CIB, have important implications for both cosmology and astrophysics. Some applications include: (a) probing astrophysical feedback processes, which may, in turn, help in shedding light on the origin of the S_8 tension (C. Preston et al. 2023); (b) understanding the gas physics necessary to properly model the ICM pressure profiles (N. Battaglia et al. 2012); (c) constraining the kSZ power spectrum through priors on tSZ power spectrum amplitude and the shape of the tSZ \times CIB (E. M. George et al. 2015, R21); (d) calibrating multi-tracer cosmological simulations (G. Stein et al. 2020; Y. Omori 2024; T. Yang et al. 2025), which are necessary for analyzing current and next-generation datasets; and (e) constraining structure formation and probing the diffuse hot gas in large-scale structures using cross-correlations with lensing and other tracers of the dark matter field. As a result, the tSZ power spectrum measurements and the maps presented in this work have a wide variety of applications, and this work also lays the groundwork for studies from upcoming data releases from SPT-3G (K. Prabhu et al. 2024) and Simons Observatory (M. Abitbol et al. 2025).

DATA PRODUCTS AND AVAILABILITY

We release the tSZ maps and bandpowers along with the associated products and plotting scripts used in this work. They can be downloaded from this [gitrepo](#) and this [SPT_data_link](#).

ACKNOWLEDGMENTS

SR dedicates this work to the loving memory of Eric Baxter—esteemed colleague, friend, and mentor—whose significant contributions to the study of CMB secondaries and cross-correlations were invaluable.

We thank Ian McCarthy for providing the FLAMINGO power spectrum curves for various astrophysical feedback and cosmological models.

SR acknowledges support by the Illinois Survey Science Fellowship from the Center for AstroPhysical Surveys at the National Center for Supercomputing Applications; support of Michael and Ester Vaida, and the National Science Foundation via award OPP-1852617; and also the support from Universities Research Association’s Visiting Scholars Program fellowship.

This work made use of the following computing resources: Illinois Campus Cluster, a computing resource that is operated by the Illinois Campus Cluster Program (ICCP) in conjunction with the National Center for Supercomputing Applications (NCSA) and which is supported by funds from the University of Illinois Urbana-Champaign; the computational and storage services associated with the Hoffman2 Shared Cluster provided by UCLA Institute for Digital Research and Education’s

Research Technology Group; OSG Consortium ([OSG](#) 2006; [R. Pordes et al. 2007a,b](#); [I. Sfiligoi et al. 2009](#)), which is supported by the National Science Foundation awards #2030508 and #2323298; and the computing resources provided on Crossover, a high-performance computing cluster operated by the Laboratory Computing Resource Center at Argonne National Laboratory.

The South Pole Telescope program is supported by the National Science Foundation (NSF) through awards OPP-1852617 and OPP-2332483. Partial support is also provided by the Kavli Institute of Cosmological Physics at the University of Chicago. Argonne National Laboratory’s work was supported by the U.S. Department of Energy, Office of High Energy Physics, under contract DE-AC02-06CH11357. The UC Davis group acknowledges support from Michael and Ester Vaida. Work at the Fermi National Accelerator Laboratory (Fermilab), a U.S. Department of Energy, Office of Science, Office of High Energy Physics HEP User Facility, is managed by Fermi Forward Discovery Group, LLC, acting under Contract No. 89243024CSC000002. The Melbourne authors acknowledge support from the Australian Research Council’s Discovery Project scheme (No. DP210102386). The Paris group has received funding from the European Research Council (ERC) under the European Union’s Horizon 2020 research and innovation program (grant agreement No 101001897), and funding from the Centre National d’Etudes Spatiales. The SLAC group is supported in part by the Department of Energy at SLAC National Accelerator Laboratory, under contract DE-AC02-76SF00515.

APPENDIX

A. SYSTEMATIC UNCERTAINTIES

In this section, we describe our techniques for estimating systematic errors due to incorrect estimation of the expectation spectra, calibration errors, and imperfect knowledge of the experimental beam.

A.1. *Systematic uncertainty in the expectation spectra*

Misestimation of the undesired components will lead to a bias in the final tSZ estimate. In this section, we perform a set of systematic checks, using analytical and simulation-based methods, to ensure that the tSZ-only power spectra we report are robust against the systematics from these contaminating signals. We show the expected contribution from each of these components as colored bands in the top panels of Fig. 3: CMB in yellow, CIB in red, kSZ in green and radio in blue. The bands correspond to the range of possible values for each component and indicate the systematic error associated

with the misestimation of each of them. We obtain the residuals and the systematic error bands as follows.

A.1.1. *CMB residuals*

We compute the CMB residual using CMB-only simulations of the Λ CDM power spectrum. As shown by the yellow curve in Fig. 3, the CMB residuals peak around $\ell \sim 3000$, with an amplitude of $D_{\ell}^{yy, \text{CMB-res}} \approx 0.5 \times 10^{-12}$. This peak is roughly near the peak of the expected tSZ power spectrum ([I. G. McCarthy et al. 2014](#), for example), although we note that the exact amplitude and the shape of the tSZ power spectrum is unknown. The residuals are nearly the same for all of the spectra combinations shown in Fig. 3.

To calculate the systematic errors due to misestimation of the CMB residual, we use the SPT-3G (from the 2018 season) and *Planck* chains ([L. Balkenhol et al. 2023](#)) to sample the cosmological parameters randomly.

Besides the Λ CDM parameters, the chains also contain the T_{Cal} factors for SPT-3G's 95, 150, and 220 GHz bands, which we also include. We assume an absolute calibration error of 0.5% and 5% respectively for the SPTpol (J. W. Henning et al. 2018; T.-L. Chou et al. 2025) and *Herschel*-SPIRE (M. P. Viero et al. 2019) bands. For each sample, i , we obtain the CMB power spectrum using CAMB software (A. Lewis et al. 2000) and estimate the corresponding CMB residual in the total measured power spectrum as given in Eq.(A1) (RO23)

$$C_{\ell, \text{ILC}}^{\text{CMB},i} = w_{\ell_A} \mathbf{C}_{\ell}^{\text{CMB},i} w_{\ell_B}^{\dagger} \quad (\text{A1})$$

where $\mathbf{C}_{\ell}^{\text{CMB},i}$ is the $N_{\text{band}} \times N_{\text{band}}$ matrix containing the CMB power spectra between different frequency bands for the i^{th} sample and the frequency-dependent LC weights corresponding to $A, B \in [\text{MV}, \text{CIB-min}]$ are w_{ℓ} . This approach, which uses the sampled power spectra to compute residuals rather than a full map-based simulation, ignores the sample variance in the systematic errors. However, this is expected to have no impact given how small the systematic errors are. We also note that the results of L. Balkenhol et al. (2023) constrained cosmology using information only up to $\ell = 3000$. Consequently, any impact on the CMB spectra arising from differences in cosmological parameters at smaller scales will not be taken into account here. However, since the systematic error from the CMB is sub-dominant relative to the other signals at these scales, it should have no impact on our results.

A.1.2. CIB residuals

Next, we compute the CIB residuals and the associated systematics using AGORA simulations. The CIB residuals peak around $\ell \sim 2000$, with an amplitude of $D_{\ell}^{yy, \text{CIB-res}} \approx 0.5 \times 10^{-12}$, for both the MV and CIB-min cases, but the residuals are reduced significantly to $D_{\ell}^{yy, \text{CIB-res}} \leq 0.1 \times 10^{-12}$ at $\ell \geq 2500$, which is much smaller than the expected level of tSZ. This is due to the low-noise 220 GHz data from SPT-3G and the addition of the high frequency *Herschel*-SPIRE data. While the residual level is generally smaller for the CIB-min spectra compared to the MV as expected, the residual levels become comparable for the two maps at $\ell \geq 2000$. Since CIB dominates the small scale power, the LC weights for MV are tuned to suppress CIB efficiently, resulting in very low residuals, similar to the CIB-min case.

To get the systematic error band, we take the CIB-only portion of the AGORA simulations and multiply the map in each SPT band independently with a factor sampled from a normal distribution, $\mathcal{N}(1, \sigma^2)$, with $\sigma = \sqrt{0.2}$. To be more specific, the scaling modifies the auto- and cross-power spectra of the CIB in each

frequency band independently, which introduces decorrelation in the CIB between different bands. Since the CIB power has been measured at very high significance ($\sim 25 - 35\sigma$), particularly on small-scales, by both ACT (T. Louis et al. 2025) and SPT (R21), the 20% variance used for this exercise is a conservative estimate. This random scaling of the maps introduces a scatter in the CIB SED for each simulation. Since the LC weights are fixed, this leads to an estimation of the CIB residual in each simulation that is different from our baseline setup. We perform this scaling 100 times, and the red band in Fig. 3 shows the resulting spread in the CIB residuals. We note that this process gives a higher level of residual compared to scaling all the bands up or down by the same factor. Note that, in the above procedure, we have not scaled the CIB power in *Herschel*-SPIRE bands, since the CIB power has been measured with extremely high S/N in those bands, and the simulations we use are calibrated to match the CIB power measured by *Herschel*-SPIRE. If we also tweak the CIB power in *Herschel*-SPIRE bands, then the width of the band increases by $\sim 15 - 20\%$ at all scales. Similarly, if we introduce a 30% scatter, we observe that the width of the band increases by $\sim 45\%$. Finally, for this exercise, we have ignored the sample variance in CIB and have only tweaked a single AGORA CIB realization since we find that the scatter between different realizations is negligible, $\times 2.5$ smaller, compared to the scatter because of the above scaling.

A.1.3. Radio residuals

We follow the same setup as described above for the CIB and assume a 20% scatter to quantify the radio residuals and the associated systematics. This assumption is conservative, given the measurement errors in the radio power reported by (E. M. George et al. 2015, R21), and T. Louis et al. (2025). In addition, we have examined the radio power under modifications to the underlying source counts (see below) and find that the resulting change is much smaller than the assumed scatter. The residuals are obtained using the radio-only portion of AGORA, and the systematic band, shown as blue in Fig.3, is obtained by scaling the maps from individual frequency bands. The radio residuals tend to increase with multipole with $D_{\ell}^{yy, \text{Rad-res}} = 0.1 (0.35) \times 10^{-12}$ at $\ell = 3000$ (5000) for all the three panels in the figure.

For radio residuals, in addition to using the AGORA simulations, we also perform an additional analytical test by modifying the underlying source counts, dN/dS . Note that the radio source counts in the AGORA simulations are shown to match the results from G. Lagache et al. (2020). We use Eq.(A1) based on the prescription

in §3.2 of RO23 and calculate the expected radio residuals. The C_ℓ^{CMB} in Eq.(A1) is replaced by C_ℓ^{Radio} as given in Eq.(A2) for three different dN/dS distributions: [de Zotti](#) ([G. De Zotti et al. 2005](#)), [Tucci](#) ([M. Tucci et al. 2011](#)), and [Lagache](#) ([G. Lagache et al. 2020](#)) as given below:

$$C_{\ell_{\nu_1 \nu_2}}^{\text{Radio}} = \int_{\alpha_{\text{rad}}^{\text{min}}}^{\alpha_{\text{rad}}^{\text{max}}} d\alpha \int_0^{S_{150}^{\text{max}}} dS_{150} S_{150}^2 \frac{dN}{dS_{150}} \left(\frac{\nu_0^2}{\nu_1 \nu_2} \right)^\alpha \mathcal{N} [\alpha_{\text{rad}} | \bar{\alpha}_{\text{rad}}, \sigma(\alpha_{\text{rad}})], \quad (\text{A2})$$

with flux threshold $\nu_0 = 150$ GHz, $S_{150}^{\text{max}} = 2$ mJy, and spectral index $\alpha_{\text{rad}} = -0.76$ with a conservative scatter of $\sigma(\alpha_{\text{rad}}) = 0.6$ ([W. B. Everett et al. 2020, R21](#)). We do not show these results in Fig. 3 to avoid cluttering. As mentioned above, the source number counts of radio galaxies in AGORA matches the results from [G. Lagache et al. \(2020\)](#) to within 10% ([Y. Omori 2024](#)), and we also find that the results for [Lagache](#) is within the blue band of Fig. 3. The residuals are slightly lower for [de Zotti](#) and [Tucci](#) with the latter giving the lowest radio residual. However, the difference in the radio residuals between the three source count distributions is much smaller than the blue band obtained using the scalings above. The difference in the radio residuals from the three source count distributions compared to the width of the blue band is $\leq 5\%$ at $\ell = 3000$ and increases to $\sim 50\%$ at $\ell = 5000$.

A.1.4. *kSZ residuals*

The baseline kSZ residuals are obtained using AGORA simulations with a kSZ power that is roughly flat in D_ℓ with an amplitude $D_\ell^{\text{kSZ}} = 3 \mu\text{K}^2$. The kSZ residuals are nearly the same for all the spectra and roughly correspond to $D_\ell^{yy, \text{kSZ-res}} = 0.05 (0.2) \times 10^{-12}$ at $\ell = 3000$ (5000).

However, since the kSZ power spectrum has not been detected at high significance, we calculate the systematic from kSZ mismodeling analytically using the same procedure as the one for the CMB described above in Eq.(A1). To this end, we replace the above kSZ amplitude with a uniform distribution $D_\ell^{\text{kSZ}} \in \mathcal{U}(0, 4) \mu\text{K}^2$. We repeat this exercise 100 times and obtain the green band in Fig. 3.

A.2. *Calibration errors*

To take into account the effect of uncertainties in the absolute calibration, we randomly multiply the maps from all the bands in the simulation with a factor sampled from a normal distribution, $\mathcal{N}(1, \sigma_{\text{Calib}}^2)$. The calibration errors were set to be: 0.5% for SPTpol and

[Zotti](#) ([G. De Zotti et al. 2005](#)), [Tucci](#) ([M. Tucci et al. 2011](#)), and [Lagache](#) ([G. Lagache et al. 2020](#)) as given below:

SPT-3G maps (i.e., $\sigma_{\text{Calib}} = 0.005$ based on [J. W. Henning et al. 2018](#); [L. Balkenhol et al. 2023](#); [E. Camphuis et al. 2025](#)) and 5% for *Herschel*-SPIRE maps ([B. M. Swinney et al. 2010](#); [M. P. Viero et al. 2019](#)). We perform the above operation 100 times and estimate the resulting scatter. This scatter, shown using purple color in the bottom panel of Fig. 3, is taken into account in the systematic errors along with the uncertainties from the other astrophysical components described above.

A.3. *Uncertainties in beam estimation*

In this subsection, we investigate the effect of uncertainties in the experimental beam, B_ℓ , on the measured tSZ power spectra.

A.3.1. *Beam chromaticity*

As described in §2.1 and §2.2, we deconvolve the CMB beam, B_ℓ^{CMB} , from the maps before the LC step. To account for the variation of the beam across frequencies for different foreground signals, we convolve these signals with their respective component-dependent beams in the simulations. Before the LC step, similar to data, we also deconvolve the B_ℓ^{CMB} from the simulations to mimic the data. Alternatively, if we convolve all foreground signals with B_ℓ^{CMB} ignoring SED variations, we observe a scale-dependent trend. The impact, however, is small with a mean shift of $\sim 0.2\sigma$ and a maximum shift of about $\lesssim 0.3 - 0.4\sigma$ around $\ell \sim 2000$ depending on which combination of LC maps is used in the spectrum.

A.3.2. *Beam uncertainties*

As a reminder, the SPT beams are composite real-space beams constructed by combining dedicated sets of planets and point source observations. We use stacks of point sources in regions where detector nonlinearities affect the planet scans ([D. Dutcher et al. 2021](#), N. Huang et al., in preparation). In this subsection, we quantify how uncertainties in the SPT beam estimation $\sigma(B_\ell)$ propagate into our results. These uncertainties arise

both from noise-induced scatter and from systematic effects associated with the choice of radius used when combining planet and point source observations to construct the composite beam (N. Huang et al., in preparation). For this test, we alter the component-dependent beams used in the simulation as $B_\ell^{\text{comp}} \rightarrow B_\ell^{\text{comp}} + \sigma(B_\ell^{\text{comp}})$ while deriving the expectation signal for the undesired components. The CMB beam without the additional

shift B_ℓ^{CMB} is deconvolved from the simulations before the LC step. Similar to the case above, the final tSZ estimates also show a slight scale-dependent trend. The maximum shift is in the first bin which moves up $\sim 0.5\sigma$ but the impact is much smaller for the other bins: $\leq 0.25\sigma$ for $\ell \leq 3000$ and $\leq 0.1\sigma$ for $\ell > 3000$. The average shift is $\leq 0.15\sigma$ for all LC estimates.

REFERENCES

Abitbol, M., Abril-Cabezas, I., Adachi, S., et al. 2025, *JCAP*, 2025, 034, doi: [10.1088/1475-7516/2025/08/034](https://doi.org/10.1088/1475-7516/2025/08/034)

Anbajagane, D., Chang, C., Jain, B., et al. 2022, *MNRAS*, 514, 1645, doi: [10.1093/mnras/stac1376](https://doi.org/10.1093/mnras/stac1376)

Archipley, M., Hryciuk, A., Bleem, L. E., et al. 2026, *A&A*, 706, A17, doi: [10.1051/0004-6361/202555798](https://doi.org/10.1051/0004-6361/202555798)

Austermann, J. E., Aird, K. A., Beall, J. A., et al. 2012, in *Proc. SPIE*, Vol. 8452, Society of Photo-Optical Instrumentation Engineers (SPIE) Conference Series, doi: [10.1117/12.927286](https://doi.org/10.1117/12.927286)

Balkenhol, L., Dutcher, D., Spurio Mancini, A., et al. 2023, *PhRvD*, 108, 023510, doi: [10.1103/PhysRevD.108.023510](https://doi.org/10.1103/PhysRevD.108.023510)

Battaglia, N., Bond, J. R., Pfrommer, C., & Sievers, J. L. 2012, *ApJ*, 758, 75, doi: [10.1088/0004-637X/758/2/75](https://doi.org/10.1088/0004-637X/758/2/75)

Baxter, E. J., & Sherwin, B. D. 2021, *MNRAS*, 501, 1823, doi: [10.1093/mnras/staa3706](https://doi.org/10.1093/mnras/staa3706)

Bender, A. N., Ade, P. A. R., Ahmed, Z., et al. 2018, in *Proc. SPIE*, Vol. 10708, *Proc. SPIE*, 1070803, doi: [10.1117/12.2312426](https://doi.org/10.1117/12.2312426)

Benoit-Lévy, A., Déchelette, T., Benabed, K., et al. 2013, *A&A*, 555, A37, doi: [10.1051/0004-6361/201321048](https://doi.org/10.1051/0004-6361/201321048)

Benson, B. A., Church, S. E., Ade, P. A. R., et al. 2004, *ApJ*, 617, 829, doi: [10.1086/425677](https://doi.org/10.1086/425677)

Benson, B. A., Ade, P. A. R., Ahmed, Z., et al. 2014, in *Proc. SPIE*, Vol. 9153, Millimeter, Submillimeter, and Far-Infrared Detectors and Instrumentation for Astronomy VII, 91531P, doi: [10.1117/12.2057305](https://doi.org/10.1117/12.2057305)

Blanchard, A., & Schneider, J. 1987, *A&A*, 184, 1

Bleem, L. E., Stalder, B., de Haan, T., et al. 2015, *ApJS*, 216, 27, doi: [10.1088/0067-0049/216/2/27](https://doi.org/10.1088/0067-0049/216/2/27)

Bleem, L. E., Bocquet, S., Stalder, B., et al. 2020, *ApJS*, 247, 25, doi: [10.3847/1538-4365/ab6993](https://doi.org/10.3847/1538-4365/ab6993)

Bleem, L. E., Crawford, T. M., Ansarinejad, B., et al. 2022, *ApJS*, 258, 36, doi: [10.3847/1538-4365/ac35e9](https://doi.org/10.3847/1538-4365/ac35e9)

Bleem, L. E., Klein, M., Abbot, T. M. C., et al. 2024, *The Open Journal of Astrophysics*, 7, 13, doi: [10.21105/astro.2311.07512](https://doi.org/10.21105/astro.2311.07512)

Bocquet, S., Grandis, S., Bleem, L. E., et al. 2024, *PhRvD*, 110, 083510, doi: [10.1103/PhysRevD.110.083510](https://doi.org/10.1103/PhysRevD.110.083510)

Bolliet, B., Comis, B., Komatsu, E., & Macías-Pérez, J. F. 2018, *MNRAS*, 477, 4957, doi: [10.1093/mnras/sty823](https://doi.org/10.1093/mnras/sty823)

Butler, V. L., Feder, R. M., Daylan, T., et al. 2022, *ApJ*, 932, 55, doi: [10.3847/1538-4357/ac6c04](https://doi.org/10.3847/1538-4357/ac6c04)

Camphuis, E., Quan, W., Balkenhol, L., et al. 2025, *arXiv e-prints*, arXiv:2506.20707, doi: [10.48550/arXiv.2506.20707](https://doi.org/10.48550/arXiv.2506.20707)

Cardoso, J.-F., Le Jeune, M., Delabrouille, J., Betoule, M., & Patanchon, G. 2008, *IEEE Journal of Selected Topics in Signal Processing*, 2, 735, doi: [10.1109/JSTSP.2008.2005346](https://doi.org/10.1109/JSTSP.2008.2005346)

Chandran, J., Remazeilles, M., & Barreiro, R. B. 2023, *MNRAS*, 526, 5682, doi: [10.1093/mnras/stad3156](https://doi.org/10.1093/mnras/stad3156)

Chaubal, P., Huang, N., Reichardt, C. L., et al. 2026, *arXiv e-prints*, arXiv:2601.20551, <https://arxiv.org/abs/2601.20551>

Chou, T.-L., Ade, P. A. R., Anderson, A. J., et al. 2025, *PhRvD*, 111, 123513, doi: [10.1103/PhysRevD.111.123513](https://doi.org/10.1103/PhysRevD.111.123513)

Coulton, W., Madhavacheril, M. S., Duivenvoorden, A. J., et al. 2024, *PhRvD*, 109, 063530, doi: [10.1103/PhysRevD.109.063530](https://doi.org/10.1103/PhysRevD.109.063530)

Dalal, N., To, C.-H., Hirata, C., et al. 2025, *arXiv e-prints*, arXiv:2507.04476, doi: [10.48550/arXiv.2507.04476](https://doi.org/10.48550/arXiv.2507.04476)

Das, S., Chiang, Y.-K., & Mathur, S. 2023, *ApJ*, 951, 125, doi: [10.3847/1538-4357/acd764](https://doi.org/10.3847/1538-4357/acd764)

Das, S., Sherwin, B. D., Aguirre, P., et al. 2011, *Physical Review Letters*, 107, 021301, doi: [10.1103/PhysRevLett.107.021301](https://doi.org/10.1103/PhysRevLett.107.021301)

De Zotti, G., Ricci, R., Mesa, D., et al. 2005, *A&A*, 431, 893, doi: [10.1051/0004-6361:20042108](https://doi.org/10.1051/0004-6361:20042108)

Dunkley, J., Calabrese, E., Sievers, J., et al. 2013, *JCAP*, 7, 25, doi: [10.1088/1475-7516/2013/07/025](https://doi.org/10.1088/1475-7516/2013/07/025)

Dutcher, D., Balkenhol, L., Ade, P. A. R., et al. 2021, *PhRvD*, 104, 022003, doi: [10.1103/PhysRevD.104.022003](https://doi.org/10.1103/PhysRevD.104.022003)

Efstathiou, G., & McCarthy, F. 2025, *MNRAS*, doi: [10.1093/mnras/staf709](https://doi.org/10.1093/mnras/staf709)

Elbers, W., Frenk, C. S., Jenkins, A., et al. 2025, *MNRAS*, 537, 2160, doi: [10.1093/mnras/staf093](https://doi.org/10.1093/mnras/staf093)

Erler, J., Basu, K., Chluba, J., & Bertoldi, F. 2018, MNRAS, 476, 3360, doi: [10.1093/mnras/sty327](https://doi.org/10.1093/mnras/sty327)

Everett, W. B., Zhang, L., Crawford, T. M., et al. 2020, ApJ, 900, 55, doi: [10.3847/1538-4357/ab9df7](https://doi.org/10.3847/1538-4357/ab9df7)

Ferraro, S., Hill, J. C., Battaglia, N., Liu, J., & Spergel, D. N. 2016, PhRvD, 94, 123526, doi: [10.1103/PhysRevD.94.123526](https://doi.org/10.1103/PhysRevD.94.123526)

George, E. M., Reichardt, C. L., Aird, K. A., et al. 2015, ApJ, 799, 177, doi: [10.1088/0004-637X/799/2/177](https://doi.org/10.1088/0004-637X/799/2/177)

Giardiello, S., Duivenvoorden, A. J., Calabrese, E., et al. 2025, PhRvD, 111, 043502, doi: [10.1103/PhysRevD.111.043502](https://doi.org/10.1103/PhysRevD.111.043502)

Griffin, M. J., Abergel, A., Abreu, A., et al. 2010, A&A, 518, L3, doi: [10.1051/0004-6361/201014519](https://doi.org/10.1051/0004-6361/201014519)

Hadzhiyska, B., Ferraro, S., Pakmor, R., et al. 2023, MNRAS, 526, 369, doi: [10.1093/mnras/stad2751](https://doi.org/10.1093/mnras/stad2751)

Henning, J. W., Sayre, J. T., Reichardt, C. L., et al. 2018, ApJ, 852, 97, doi: [10.3847/1538-4357/aa9ff4](https://doi.org/10.3847/1538-4357/aa9ff4)

Hernandez, J., Bleem, L., Crawford, T., et al. 2023, The Open Journal of Astrophysics, 6, 41, doi: [10.21105/astro.2309.12475](https://doi.org/10.21105/astro.2309.12475)

Hill, J. C., Ferraro, S., Battaglia, N., Liu, J., & Spergel, D. N. 2016, Physical Review Letters, 117, doi: [10.1103/physrevlett.117.051301](https://doi.org/10.1103/physrevlett.117.051301)

Hill, J. C., & Pajer, E. 2013, PhRvD, 88, 063526, doi: [10.1103/PhysRevD.88.063526](https://doi.org/10.1103/PhysRevD.88.063526)

Hill, J. C., & Spergel, D. N. 2014, JCAP, 2014, 030, doi: [10.1088/1475-7516/2014/02/030](https://doi.org/10.1088/1475-7516/2014/02/030)

Hilton, M., Sifón, C., Naess, S., et al. 2021, ApJS, 253, 3, doi: [10.3847/1538-4365/abd023](https://doi.org/10.3847/1538-4365/abd023)

Holder, G. P., McCarthy, I. G., & Babul, A. 2007, MNRAS, 382, 1697, doi: [10.1111/j.1365-2966.2007.12430.x](https://doi.org/10.1111/j.1365-2966.2007.12430.x)

Horowitz, B., & Seljak, U. 2017, MNRAS, 469, 394, doi: [10.1093/mnras/stx766](https://doi.org/10.1093/mnras/stx766)

Huang, N., Bleem, L. E., Stalder, B., et al. 2020, AJ, 159, 110, doi: [10.3847/1538-3881/ab6a96](https://doi.org/10.3847/1538-3881/ab6a96)

Jones, M. E., Edge, A. C., Grainge, K., et al. 2005, MNRAS, 357, 518, doi: [10.1111/j.1365-2966.2005.08626.x](https://doi.org/10.1111/j.1365-2966.2005.08626.x)

Komatsu, E., & Seljak, U. 2002, MNRAS, 336, 1256

Kornoelje, K., Bleem, L. E., Rykoff, E. S., et al. 2025, ApJ, submitted, arXiv:2503.17271, doi: [10.48550/arXiv.2503.17271](https://doi.org/10.48550/arXiv.2503.17271)

Kusiak, A., Bolliet, B., Ferraro, S., Hill, J. C., & Krolewski, A. 2021, PhRvD, 104, 043518, doi: [10.1103/PhysRevD.104.043518](https://doi.org/10.1103/PhysRevD.104.043518)

Lagache, G., Béthermin, M., Montier, L., Serra, P., & Tucci, M. 2020, A&A, 642, A232, doi: [10.1051/0004-6361/201937147](https://doi.org/10.1051/0004-6361/201937147)

Lewis, A. 2013, JCAP, 2013, 053, doi: [10.1088/1475-7516/2013/08/053](https://doi.org/10.1088/1475-7516/2013/08/053)

Lewis, A., & Challinor, A. 2006, PhR, 429, 1, doi: [10.1016/j.physrep.2006.03.002](https://doi.org/10.1016/j.physrep.2006.03.002)

Lewis, A., Challinor, A., & Lasenby, A. 2000, ApJ, 538, 473, doi: [10.1086/309179](https://doi.org/10.1086/309179)

Liu, R. H., Ferraro, S., Schaan, E., et al. 2025, arXiv e-prints, arXiv:2502.08850, doi: [10.48550/arXiv.2502.08850](https://doi.org/10.48550/arXiv.2502.08850)

Louis, T., La Posta, A., Atkins, Z., et al. 2025, arXiv e-prints, arXiv:2503.14452, doi: [10.48550/arXiv.2503.14452](https://doi.org/10.48550/arXiv.2503.14452)

Madhavacheril, M. S., Hill, J. C., Næss, S., et al. 2020, PhRvD, 102, 023534, doi: [10.1103/PhysRevD.102.023534](https://doi.org/10.1103/PhysRevD.102.023534)

Madhavacheril, M. S., Qu, F. J., Sherwin, B. D., et al. 2024, ApJ, 962, 113, doi: [10.3847/1538-4357/acff5f](https://doi.org/10.3847/1538-4357/acff5f)

McCarthy, F., & Hill, J. C. 2024, PhRvD, 109, 023529, doi: [10.1103/PhysRevD.109.023529](https://doi.org/10.1103/PhysRevD.109.023529)

McCarthy, I. G., Le Brun, A. M. C., Schaye, J., & Holder, G. P. 2014, MNRAS, 440, 3645, doi: [10.1093/mnras/stu543](https://doi.org/10.1093/mnras/stu543)

McCarthy, I. G., Amon, A., Schaye, J., et al. 2025, MNRAS, 540, 143, doi: [10.1093/mnras/staf731](https://doi.org/10.1093/mnras/staf731)

Moser, E., Battaglia, N., Nagai, D., et al. 2022, ApJ, 933, 133, doi: [10.3847/1538-4357/ac70c6](https://doi.org/10.3847/1538-4357/ac70c6)

Nagai, D., Kravtsov, A. V., & Vikhlinin, A. 2007, ApJ, 668, 1, doi: [10.1086/521328](https://doi.org/10.1086/521328)

Navarro, J. F., Frenk, C. S., & White, S. D. M. 1996, ApJ, 462, 563, doi: [10.1086/177173](https://doi.org/10.1086/177173)

Omori, Y. 2024, MNRAS, 530, 5030, doi: [10.1093/mnras/stae1031](https://doi.org/10.1093/mnras/stae1031)

Omori, Y., Chown, R., Simard, G., et al. 2017, ApJ, 849, 124, doi: [10.3847/1538-4357/aa8d1d](https://doi.org/10.3847/1538-4357/aa8d1d)

OSG. 2006, OSPool, OSG, doi: [10.21231/906P-4D78](https://doi.org/10.21231/906P-4D78)

Pandey, S., Lehman, K., Baxter, E. J., et al. 2023, MNRAS, 525, 1779, doi: [10.1093/mnras/stad2268](https://doi.org/10.1093/mnras/stad2268)

Pilbratt, G. L., Riedinger, J. R., Passvogel, T., et al. 2010, A&A, 518, L1, doi: [10.1051/0004-6361/201014759](https://doi.org/10.1051/0004-6361/201014759)

Planck Collaboration, Ade, P. A. R., Aghanim, N., et al. 2014a, A&A, 571, A21, doi: [10.1051/0004-6361/201321522](https://doi.org/10.1051/0004-6361/201321522)

Planck Collaboration, Ade, P. A. R., Aghanim, N., et al. 2014b, A&A, 571, A9, doi: [10.1051/0004-6361/201321531](https://doi.org/10.1051/0004-6361/201321531)

Planck Collaboration, Ade, P. A. R., Aghanim, N., et al. 2016a, A&A, 594, A24, doi: [10.1051/0004-6361/201525833](https://doi.org/10.1051/0004-6361/201525833)

Planck Collaboration, Aghanim, N., Arnaud, M., et al. 2016b, A&A, 594, A22, doi: [10.1051/0004-6361/201525826](https://doi.org/10.1051/0004-6361/201525826)

Planck Collaboration, Aghanim, N., Akrami, Y., et al. 2020, A&A, 641, A8, doi: [10.1051/0004-6361/201833886](https://doi.org/10.1051/0004-6361/201833886)

Polenta, G., Marinucci, D., Balbi, A., et al. 2005, *JCAP*, 11, 1, doi: [10.1088/1475-7516/2005/11/001](https://doi.org/10.1088/1475-7516/2005/11/001)

Pordes, R., Petravick, D., Kramer, B., et al. 2007a, in 78, Vol. 78, *J. Phys. Conf. Ser.*, 012057, doi: [10.1088/1742-6596/78/1/012057](https://doi.org/10.1088/1742-6596/78/1/012057)

Pordes, R., et al. 2007b, *J. Phys. Conf. Ser.*, 78, 012057, doi: [10.1088/1742-6596/78/1/012057](https://doi.org/10.1088/1742-6596/78/1/012057)

Prabhu, K., Raghunathan, S., Millea, M., et al. 2024, Testing the Λ CDM Cosmological Model with Forthcoming Measurements of the Cosmic Microwave Background with SPT-3G, arXiv, doi: [10.48550/ARXIV.2403.17925](https://doi.org/10.48550/ARXIV.2403.17925)

Preston, C., Amon, A., & Efstathiou, G. 2023, *MNRAS*, 525, 5554, doi: [10.1093/mnras/stad2573](https://doi.org/10.1093/mnras/stad2573)

Raghunathan, S. 2022, *ApJ*, 928, 16, doi: [10.3847/1538-4357/ac510f](https://doi.org/10.3847/1538-4357/ac510f)

Raghunathan, S., Holder, G. P., Bartlett, J. G., et al. 2019, *JCAP*, 2019, 037, doi: [10.1088/1475-7516/2019/11/037](https://doi.org/10.1088/1475-7516/2019/11/037)

Raghunathan, S., & Omori, Y. 2023, *ApJ*, 954, 83, doi: [10.3847/1538-4357/ace0c6](https://doi.org/10.3847/1538-4357/ace0c6)

Raghunathan, S., Ade, P. A. R., Anderson, A. J., et al. 2024, *PhRvL*, 133, 121004, doi: [10.1103/PhysRevLett.133.121004](https://doi.org/10.1103/PhysRevLett.133.121004)

Reichardt, C. L., Patil, S., Ade, P. A. R., et al. 2021, *ApJ*, 908, 199, doi: [10.3847/1538-4357/abd407](https://doi.org/10.3847/1538-4357/abd407)

Remazeilles, M., Delabrouille, J., & Cardoso, J.-F. 2011, *MNRAS*, 410, 2481, doi: [10.1111/j.1365-2966.2010.17624.x](https://doi.org/10.1111/j.1365-2966.2010.17624.x)

Sánchez, J., Omori, Y., Chang, C., et al. 2023, *MNRAS*, doi: [10.1093/mnras/stad1167](https://doi.org/10.1093/mnras/stad1167)

Schaan, E., Ferraro, S., Amodeo, S., et al. 2021, *PhRvD*, 103, 063513, doi: [10.1103/PhysRevD.103.063513](https://doi.org/10.1103/PhysRevD.103.063513)

Schaffer, K. K., Crawford, T. M., Aird, K. A., et al. 2011, *ApJ*, 743, 90, doi: [10.1088/0004-637X/743/1/90](https://doi.org/10.1088/0004-637X/743/1/90)

Schaye, J., Kugel, R., Schaller, M., et al. 2023, *MNRAS*, 526, 4978, doi: [10.1093/mnras/stad2419](https://doi.org/10.1093/mnras/stad2419)

Sfiligoi, I., Bradley, D. C., Holzman, B., et al. 2009, in 2, Vol. 2, 2009 WRI World Congress on Computer Science and Information Engineering, 428–432, doi: [10.1109/CSIE.2009.950](https://doi.org/10.1109/CSIE.2009.950)

Shaw, L. D., Holder, G. P., & Dudley, J. 2010, *ApJ*, 716, 281, doi: [10.1088/0004-637X/716/1/281](https://doi.org/10.1088/0004-637X/716/1/281)

Smith, K. M., Zahn, O., & Doré, O. 2007, *PhRvD*, 76, 043510, doi: [10.1103/PhysRevD.76.043510](https://doi.org/10.1103/PhysRevD.76.043510)

Sobrin, J. A., Anderson, A. J., Bender, A. N., et al. 2022, *ApJS*, 258, 42, doi: [10.3847/1538-4365/ac374f](https://doi.org/10.3847/1538-4365/ac374f)

Staniszewski, Z., Ade, P. A. R., Aird, K. A., et al. 2009, *ApJ*, 701, 32, doi: [10.1088/0004-637X/701/1/32](https://doi.org/10.1088/0004-637X/701/1/32)

Stein, G., Alvarez, M. A., Bond, J. R., van Engelen, A., & Battaglia, N. 2020, *JCAP*, 2020, 012, doi: [10.1088/1475-7516/2020/10/012](https://doi.org/10.1088/1475-7516/2020/10/012)

Sunyaev, R., & Zel'dovich, Y. 1980, *ARAA*, 18, 537, doi: [10.1146/annurev.aa.18.090180.002541](https://doi.org/10.1146/annurev.aa.18.090180.002541)

Sunyaev, R. A., & Zeldovich, Y. B. 1980, *MNRAS*, 190, 413. http://adsabs.harvard.edu/cgi-bin/nph-bib_query?bibcode=1980MNRAS.190..413S&db_key=AST

Swinyard, B. M., Ade, P., Baluteau, J.-P., et al. 2010, *A&A*, 518, L4, doi: [10.1051/0004-6361/201014605](https://doi.org/10.1051/0004-6361/201014605)

Tanimura, H., Douspis, M., Aghanim, N., & Salvati, L. 2022, *MNRAS*, 509, 300, doi: [10.1093/mnras/stab2956](https://doi.org/10.1093/mnras/stab2956)

Torrado, J., & Lewis, A. 2021, *JCAP*, 2021, 057, doi: [10.1088/1475-7516/2021/05/057](https://doi.org/10.1088/1475-7516/2021/05/057)

Tristram, M., Macías-Pérez, J. F., Renault, C., & Santos, D. 2005, *MNRAS*, 358, 833, doi: [10.1111/j.1365-2966.2005.08760.x](https://doi.org/10.1111/j.1365-2966.2005.08760.x)

Tucci, M., Toffolatti, L., de Zotti, G., & Martínez-González, E. 2011, *A&A*, 533, A57, doi: [10.1051/0004-6361/201116972](https://doi.org/10.1051/0004-6361/201116972)

Viero, M. P., Reichardt, C. L., Benson, B. A., et al. 2019, *ApJ*, 881, 96, doi: [10.3847/1538-4357/ab2da0](https://doi.org/10.3847/1538-4357/ab2da0)

Yang, T., McCarthy, I. G., McCarthy, F., et al. 2025, arXiv e-prints, arXiv:2512.09891, doi: [10.48550/arXiv.2512.09891](https://doi.org/10.48550/arXiv.2512.09891)